Quantitative Models of AGB Populations with Subsolar Metallicities and their Mass Loss

vorgelegt von
Dipl.-Phys.
Astrid Wachter
aus Weißenburg

Von der Fakultät II - Mathematik und Naturwissenschaften
der Technischen Universität Berlin

zur Erlangung des akademischen Grades

Doktor der Naturwissenschaften
– Dr. rer. nat. –

genehmigte Dissertation

Promotionsausschuss:

Vorsitzender: Prof. Dr. Hans Joachim Eichler
Berichter/Gutachter: Prof. Dr. Erwin Sedlmayr
Berichter/Gutachter: Prof. Dr. Heike Rauer

Tag der wissenschaftlichen Aussprache: 16.02.2007

Berlin 2007

D 83

Contents

List of Figures

List of Tables

Chapter 1

Introduction

In this work the mass loss of stars is investigated with special focus on those populating the asymptotic giant branch (AGB) in the Hertzsprung-Russell diagram characterised by high luminosities and low effective temperatures. On the AGB stars with low- and intermediate main sequence (=initial) mass ($\sim$1 ... 8 $M_\odot$, solar masses)[1] are in their late stage of evolution. This phase is characterised by instabilities leading to stellar pulsations as observed in long-period variables (LPVs) or Mira stars. Cioni et al. (2001), for instance, found that 65% of the stars in the considered sample of giants in the Large Magellanic Cloud (LMC) are LPVs. Furthermore, this phase is connected to strong mass-loss of more than a few $10^{-5}\,M_\odot$ yr^{-1}, for which Renzini (1981) suggested the terminus "superwind". By means of their mass loss, these stars contribute enormously to the enrichment of the interstellar matter with material processed through nuclear burning reactions (for a review on nucleosynthesis in AGB stars see e.g. Busso et al. 1999) and dust, and are therefore not only interesting as objects of stellar evolution but also in terms of galactic chemical evolution.

Several reviews have approached the fascinating topic of AGB stars over the years. Iben & Renzini (1983) and Herwig (2005) for example focus on the theoretical aspects by summarising stellar evolution modeling. Habing (1996) gives a general overview of AGB star research at that time, which recently has been updated and extended in the monograph by Habing & Olofsson (2004), where important issues like nucleosynthesis and evolution, atmospheres, circumstellar envelopes, molecule and dust grain formation, and more are presented by several authors. More specific topics concerning AGB stars have been addressed in further reviews, like for instance the s-process (Busso et al. 1999) and carbon stars in general (Wallerstein & Knapp 1998). Mechanisms for mass-loss of evolved stars are discussed in Lafon & Berruyer (1991), while Willson (2000) gives an overview of observational mass-loss determinations and empirical mass-loss formulae, just to name a

[1] The precise values depend on the initial element abundances / metallicity and are as well model dependent.

few. In the following, I compile only some main characteristics and features, which are related to this work.

Starting with some recent observational determinations of stellar quantities of giants and in particular Mira stars, which are pulsating late type stars with effective temperatures lower than 4000 K and high luminosities, Alvarez & Mennessier (1997) for instance investigated 165 oxygen-rich Miras, for which they determined effective temperatures in the range ∼2500 ... 3400 K, luminosities of ∼1400 ... 4700 $L_{\odot}$, and periods of 150... 550 d. Bergeat & Chevallier (2005) used millimetre observations of 119 carbon-rich giants (thereof 19 Miras) and found $T_{\rm eff}$ of 1800 ... 3400 (1800 ... 3200) K, luminosities of 1700 ... 21000 (2300 ... 18000) $L_{\odot}$, mass-loss rates of 1.5×10^{-8} ... 3.3×10^{-5} (1.0×10^{-7} ... 3.3×10^{-5}) $M_{\odot}$ yr^{-1}, and C/O ratios of 1.01 ... 1.8 (1.01 ... 1.4[2]).

It is well established that AGB stars undergo substantial mass loss, whereby circumstellar envelopes consisting of gas and dust are formed (Olofsson et al. 1990). In a manner of speaking, IRC+10216 is the prototype of mass-losing carbon stars with a mass-loss rate of $\sim 3 \times 10^{-5}$ $M_{\odot}$ yr^{-1}. If the mass loss is changing with time, i.e. if after a period of strong mass loss its rate drops, these envelopes can develop onion-like shells. A well-known example for such episodic mass loss event is the detached CO shell of TT Cyg observed by Olofsson et al. (2000). Showing such high mass-loss rates, low- and intermediate mass stars are important contributors to the cosmic cycle of matter, especially since these stars are far more numerous than high mass stars which end their lives in supernova explosions. Besides, due to their shorter lifetimes the latter contribute to the material enrichment mainly in younger stellar systems.

As already stated, the AGB stage is a late phase of stellar evolution. The star has already burned its hydrogen fuel in the core (on the main sequence, the longest evolutionary stage) to helium, and has become a red giant due to subsequent expansion of the stellar envelope and simultaneous contraction of the He-core. It has as well ignited core He-burning and consumed the helium in its core. The interior structure of an AGB star consists of a carbon-oxygen core supported by the pressure of degenerate electrons surrounded by a helium and hydrogen shell. In a star more massive than ∼8 $M_{\odot}$ the temperature is high enough, so that the electron gas in the C-O core never degenerates. Consequently, instead of experiencing the AGB phase such a star starts further nuclear fusion process(es) and eventually ends its life as a supernova, being either totally destroyed or leaving a neutron star or black hole as remnant[3]. The presence of the two burning shells in an AGB star

[2]These data are obtained only for 4 Miras.

[3]Again, the actual fate is determined by the current stellar mass which can be traced back to the initial main sequence mass, and is therefore model dependent.

leads to interesting effects like thermal pulses and a third dredge-up phase, which are most important for the formation of carbon stars.

In the atmosphere of an AGB star, the existence of dust has an immense influence on its physics and chemistry. Once dust is formed, it plays an important role as driving-mechanism of the mass loss, because its absorption cross section is by far larger than that of the (molecular) gas. Due to the pulsation the stellar atmosphere is levitated leading to favourable conditions for dust formation. The radiation pressure on the formed dust grains and the frictional coupling between the dust and surrounding gas accelerates the material outwards and results in a substantial stellar mass loss. Of course there exist other driving-mechanisms of stellar winds like energy input via sound waves or influence of magnetic fields (see Lamers & Cassinelli 1999, for an introduction to stellar winds and different processes involved), which might be of importance in cool stars' atmospheres as well, but undoubtedly radiation pressure on dust grains prevails if present. A review on dust formation itself is given by Sedlmayr (1994).

Mass loss itself is not an outcome of stellar evolution calculations, but needs to be prescribed within the modelling procedure. For that purpose a mass-loss description is needed which depends on stellar quantities only. Reimers (1975) presented an empirical formula for K giants in our galaxy (i.e. for stars which have not yet reached the AGB phase). For lack of a better description, this formula has subsequently been in use on the AGB as well, despite the different driving-mechanisms. In doing so, the original calibration factor "η" needed to be modified and was enhanced greatly.

In this work we theoretically investigate mass loss resulting from stellar evolution simulation in combination with a mass-loss description based on detailed dust-driven wind models. An excellent overview of the physics involved in modelling these winds is given by Sedlmayr & Winters (1991). While in earlier investigations models with solar metallicity have been evaluated, we focus here on dust-driven wind models with element abundances as observed in the Magellanic Clouds (see chapter 2). The metallicity of the Large Magellanic Cloud (LMC) is $Z = 0.008$, i.e. roughly a good third of the solar value, while the Small Magellanic Cloud (SMC) has on average an even lower metallicity of $Z = 0.004$, being half of the LMC or a fifth of the solar metallicity. Based on grids of these wind models we derive parameterised mass-loss descriptions dependent on stellar quantities only, which then have been applied to stellar evolution calculations. Those lead to a quantitative account of stellar mass loss at subsolar metallicities (chapter 3). On the basis of grids of evolutionary tracks, we are generating synthetic stellar samples which represent the present day state for a given initial mass function and star formation rate in dependence of the considered metallicity (chapter 4). These are compared to an observed sample of giants contained in the DENIS Catalogue toward Magellanic Clouds (DCMC, Cioni et al. 2000).

Chapter 2

Hydrodynamical Wind Models

In this chapter we introduce the hydrodynamical wind models from which we derive a description for the mass loss of late asymptotic giant branch (AGB) stars with less than solar metallicities. These models have been developed in the last decade by Gauger et al. (1990), Fleischer et al. (1992), and Winters et al. (1994). For (apart from the C/O abundance ratio) solar abundances, these models yield time averaged mass loss rates of up to a few 10^{-5} $M_\odot$ yr^{-1}, both for oxygen-rich and carbon-rich mixtures. This is consistent with rates inferred from, e.g. CO rotational line observations of AGB stars in the solar neighbourhood.

When considering subsolar metallicities these models show a rather quasi-static nature (Helling et al. 2002). As they already state there, this is not consistent with observations of AGB stars, e.g. in the Magellanic Clouds which indicate mass-loss rates of the same order of magnitude as they are observed at stars with solar element abundances. Therefore a reconsideration of the model assumptions seemed appropriate. We follow here the approach of dropping the model assumption of optical thick dust shells as further explained in section 2.2.6.

We present "new" models calculated with less than solar metallicities, specifically with element abundances as found in the Large and Small Magellanic Cloud.

Furthermore, approximative formulae for selected sets of models are derived that describe the wind characteristics as a function of the stellar parameters only. This restriction will be necessary for the application to stellar evolution calculations (see chapter 3).

2.1 Overall problem

Figure 2.1 sketches the overall physical problem of a stellar atmosphere. The black part represents the "classical" problem of a dust free atmosphere. The hydrodynamics is described by the equation of continuity and the equation of motion which together give the

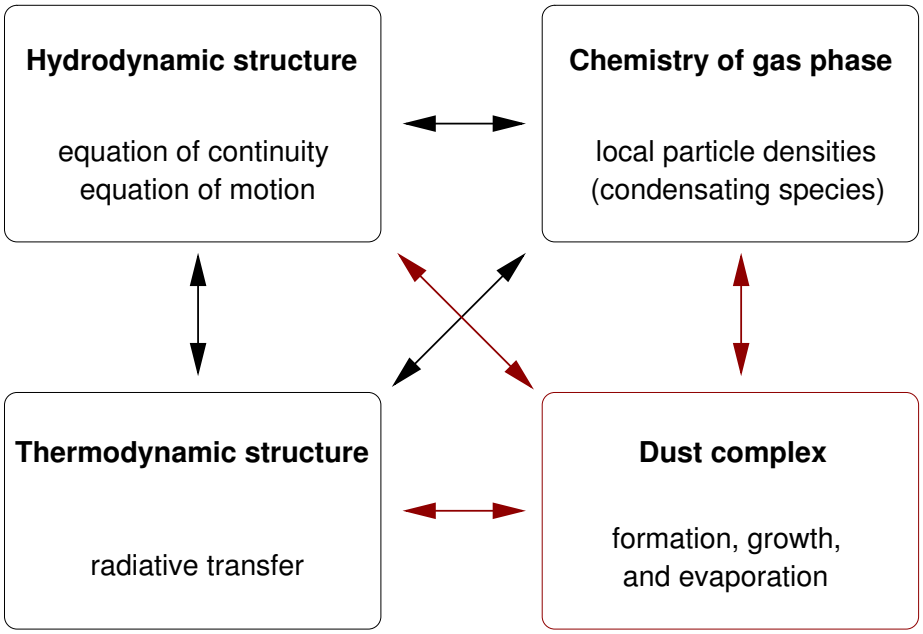

Figure 2.1: Sketch of the physics of a stellar atmosphere. The black part represents the "classical" problem of a dust free atmosphere.

density and velocity distribution. The thermodynamic structure is given by the energy equation and the radiative transfer resulting in the temperature distribution. The chemical equations yield the local densities of ions, electrons, atoms and molecules. When dust is taken into account it will influence each part of the problem.

The chemistry is influenced directly since the local densities of the gas species are reduced when dust grains are formed. The dust formation process itself is decisively dependent on the local density and temperature, since it proceeds efficiently only in a limited range of these quantities, the so-called "dust formation window". The other way around dust influences the hydro- and thermodynamic structure by its (compared to the gas) huge extinction coefficient. Radiation pressure on dust grains accelerates the grains (and via frictional coupling the surrounding gas as well) and therefore enters the equation of motion resulting in a feed-back on the hydrodynamics.

2.2 Model assumptions & basic equations

Generally, for all models in this work spherical symmetry is assumed. Contrary to the following equations (which are given in Eulerian form) Lagrangian variables, i.e. a co-moving coordinate system is used in the code to solve the equations. They have been discretised according to the scheme given in Richtmyer & Morton (1967). A detailed description of the transformation and discretisation is given in Fleischer et al. (1992) and

Fleischer (1994). Furthermore, a good summary of the latest physical ingredients[1] can be found in Schirrmacher et al. (2003).

2.2.1 Hydrodynamics

The hydrodynamical structure, i.e. the mass density ρ and outflow velocity v, follows from the equation of continuity

$$\frac{\partial \rho}{\partial t} + \frac{1}{r^2}\frac{\partial}{\partial r}(r^2 \rho v) = 0 \quad , \tag{2.1}$$

and the equation of motion

$$\frac{\partial v}{\partial t} + v\frac{\partial v}{\partial r} = -\frac{1}{\rho}\frac{\partial P}{\partial r} + a \quad , \tag{2.2}$$

with time t and radial coordinate r. The thermal pressure P is related to the density ρ and the gas temperature T via the equation of state. In our models the material is considered to be an ideal gas, i.e. the equation of state reads

$$P = \frac{\rho}{\mu m_{\mathrm{H}}} k_{\mathrm{B}} T \quad , \tag{2.3}$$

with Boltzmann constant k_{B} and mean mass per particle μ in units of the mass of the hydrogen atom m_{H}. The additional term a in eq. (2.2) includes the acceleration due to external forces. In our models it is composed of the gravitational acceleration g and the radiative acceleration a_{rad}. Typically it is written as

$$a = -g(1-\alpha) \quad , \tag{2.4}$$

where α is the ratio of radiative to gravitational acceleration ($\alpha := a_{\mathrm{rad}}/g$). The local gravitational acceleration is due to the stellar mass and the mass $M_{\mathrm{S}}(r,t) = \int_{R_\star}^{r} 4\pi r'^2 \rho(r',t) dr'$ contained inside the shell between the stellar radius $R_\star$ and r.

$$g = G\frac{M_\star + M_{\mathrm{S}}(r,t)}{r^2} \tag{2.5}$$

The expression for the radiative acceleration is

$$a_{\mathrm{rad}} = \frac{4\pi}{c}\frac{\chi_H}{\rho} H \tag{2.6}$$

with the flux-mean extinction coefficient χ_H and the frequency integrated Eddington flux H:

$$\chi_H = \frac{1}{H}\int_0^\infty \chi_\nu H_\nu d\nu \quad , \quad H = \int_0^\infty H_\nu d\nu \tag{2.7}$$

[1] The modifications presented in section 2.2.6 of this work are not yet considered there, though.

The extinction consists of contributions due to absorption (κ_ν) and scattering (σ_ν) of the material (gas and dust). If dust is present its absorption and scattering coefficients exceed those of the gas, i.e. $\kappa_\nu^{\rm d}, \sigma_\nu^{\rm d} \gg \kappa_\nu^{\rm g}, \sigma_\nu^{\rm g}$, so that it rules the interaction with the radiation field and decisively influences the hydrodynamical structure.

2.2.2 Thermodynamics

The temperature structure is determined by the law of energy conservation and the radiative transfer. The radiative equilibrium temperature results from solving the radiative transfer problem. In the present version of the code it is calculated in grey approximation using the method by Unno & Kondo (1976) in the updated version of Hashimoto (1995):

$$T_{\rm eq}^4(r) = \frac{1}{\sigma}\frac{1}{2} r_{\rm i}^2 F(r_{\rm i}) \left[\frac{1}{R^2(1+\mu_R)} + \frac{\mu_R}{R^2} - \frac{\mu_r}{r^2} + \frac{3}{2}\int_r^R (\chi_F + \frac{2\mu_{r'}}{r'})\frac{{\rm d}r'}{r'^2} \right] \tag{2.8}$$

(with Stefan-Boltzmann constant σ, location of the outer boundary R, inner boundary $r_{\rm i}$, radiative energy flux F, and flux-mean extinction coefficient χ_F) where μ_r, the cosine of the separation angle dividing the solid angle into domains with intensities $I^+(r)/I^-(r)$, is determined by

$$\frac{d\mu_r^3}{dr} = \frac{1}{4}\chi_F(r)(1-5\mu_r^2) + \frac{3\mu_r}{r}(1-\mu_r^2) \quad , \quad \mu_r(r_{\rm i}) = 0 \tag{2.9}$$

(for details see Winters et al. 1997, and references therein).

The gas energy equation reads in spherical symmetry:

$$\rho\frac{\partial e}{\partial t} + \rho v\frac{\partial e}{\partial r} + \frac{P}{r^2}\frac{\partial (r^2 v)}{\partial r} = Q_{\rm e} \tag{2.10}$$

with specific energy e, i.e. internal energy per unit mass, and local net energy input rate $Q_{\rm e}$ per unit volume due to external energy sources. Using the continuity equation (2.1) it is equivalent to the formulation

$$\frac{\partial(\rho e)}{\partial t} + \frac{1}{r^2}\frac{\partial}{\partial r}(r^2\rho v h) - v\frac{\partial P}{\partial r} = Q_{\rm e} \tag{2.11}$$

where $h = e + \frac{P}{\rho}$ is the specific enthalpy.

Shocks are treated according to Tscharnuter & Winkler (1979). They introduce a artificial viscosity to broaden the shock fronts by considering a viscous pressure tensor.

After the passage of a shock, the gas is assumed to relax radiatively towards equilibrium using a cooling law of the form

$$Q_{\rm rad} \propto \frac{\kappa_{\rm g}}{\rho}(T_{\rm eq}^4 - T_{\rm g}^4) \tag{2.12}$$

where $T_{\rm g}$ is the gas temperature.

The (grey) dust temperature $T_{\rm d}$ is set equal to the radiative equilibrium temperature $T_{\rm eq}$.

2.2.3 Chemistry

In the models considered in this work a carbon-rich mixture is assumed. The element abundances are determined assuming chemical equilibrium in the gas phase. Considered are the concentrations of species relevant for carbon grain formation, namely H, H_2, C, C_2, C_2H and C_2H_2.

Oxygen is assumed to be completely blocked in the CO molecule. Therefore the C/O ratio describes the amount of carbon available for grain formation.

2.2.4 Dust complex

The formation, growth, and evaporation of carbon grains is calculated according to the moment method by Gail & Sedlmayr (1988) and Gauger et al. (1990). There, the moments K_j of the local size distribution function $f(N,t)$ of the dust grains are defined as

$$K_j(N,t) = \sum_{N=N_{\rm l}}^{\infty} N^{j/3} \frac{f(N,t)}{n_{\rm H}} \quad , \quad j = 0, \ldots, 3 \tag{2.13}$$

with N being the number of monomers constituting the dust grain[2]. $N_{\rm l}$ is the lower limit of particle sizes.

Following from their definition, several important dust properties can be expressed in terms of these moments, like the number density of the dust $n_{\rm d}$, the degree of condensation $f_{\rm c}$, and the mean dust particle radius $\langle r \rangle$:

$$\begin{aligned} n_{\rm d} &= n_{\rm H} K_0 \\ f_{\rm c} &= \frac{n_{\rm H} K_3}{n_{\rm cond}} \\ \langle r \rangle &= a_0 \frac{K_1}{K_3} \end{aligned} \tag{2.14}$$

[2]The size of a dust grain can be described as well in terms of a particle radius $a = a_0 N^{1/3}$ with a hypothetical particle radius a_0 of the monomer.

thereby $n_{\rm cond}$ is the number density of condensable nuclei in the pure gas phase, so that $f_{\rm c}$ gives the fraction of the condensable material which is actually condensed into grains.

Since scattering is neglected in our models K_3 is the highest moment needed for the calculation of dust properties as for instance the absorption coefficient (see section 2.2.6).

The time evolution of the dust component is described by a system of differential equations for these moments:

$$\begin{aligned} \frac{dK_0}{dt} &= J(N_l,t) \\ \frac{dK_j}{dt} &= N_l^{j/3} J(N_l,t) + \frac{j}{3}\frac{1}{\tau} K_{j-1} \quad , \quad j=1,\ldots,3 \end{aligned} \tag{2.15}$$

where $J(N_l,t)$ is the net flux of particles in size-space at the lower integration boundary N_l per H atom, and $\frac{1}{\tau} = \frac{1}{\tau_{\rm grow}} - \frac{1}{\tau_{\rm evap}}$ is the net growth rate, i.e. the number of monomers which are associated/dissociated to/from a dust particle per unit time and unit surface. If the growth rate $1/\tau_{\rm grow}$ exceeds the evaporation rate $1/\tau_{\rm evap}$ then nucleation and growth takes place and $J(N_l,t)$ can be expressed by a stationary nucleation rate $J_\star$ which is dependent on the densities of the condensing species and, much stronger, on the local temperature. Otherwise dust is destroyed due to thermal evaporation and chemical sputtering and $J(N_l,t)$ is the evaporation rate. It is given by the value of the size distribution function $f(N_l,t)$ at N_l which can be inferred from the history of $J_\star$ and τ. For details see Gauger et al. (1990), and references therein.

2.2.5 Boundary conditions & input data

Each model is fully characterised by the stellar parameters mass $M_\star$, effective temperature $T_\star$, and luminosity $L_\star$, and the photospheric element abundances $\epsilon_{\rm i}$, notably the abundance ratio of carbon to oxygen. The latter distinguishes the amount of condensable material available for dust formation. The stellar radius $R_\star$ is determined by $T_\star$ and $L_\star$:

$$\frac{L_\star}{4\pi R_\star^2} = \sigma T_\star^4 \quad . \tag{2.16}$$

Inner boundary condition

The pulsation of the star is simulated by a "piston approximation", i.e. the inner boundary which is located about 10% below the stellar radius is moved sinusoidally. The calculations are started with an initially hydrostatic solution. After switching on the piston the velocity amplitude is slowly increased until the desired model value is reached. For the description of this piston the period P and the velocity amplitude $\Delta v_{\rm P}$ have to be given, i.e. these are two additional model parameters.

element	solar	LMC	SMC
H	0.00	0.00	0.00
He	-1.01	-1.06	-1.09
C	-3.40	-3.96	-4.27
O	-3.13	-3.65	-3.97

Table 2.1: Logarithmic element abundances $\log_{10}(\frac{n_{\rm el}}{n_{\rm H}})$ (cf. Helling et al. (2000)).

The radiative energy flux at the inner boundary $F(r_{\rm i})$ is set to be constant in time:

$$F(r_{\rm i}) = \frac{L_\star}{4\pi r_{\rm i}^2} = \frac{L_0}{4\pi r_0^2} = {\rm const}_t \tag{2.17}$$

Element abundances

Arndt et al. (1997) and Winters et al. (1997) have investigated models with otherwise solar abundances. In this work we consider models with subsolar metallicities, as they are observed e.g. in the Magellanic Clouds, whereat the SMC has the lower metallicity. The values for the element abundances are set as summarised by Helling et al. (2000) in their table A.1 (see also table 2.1 for the main abundances H, He, C, and O).

In the solar case, a value of $\mu = 1.26$ (in units of the hydrogen mass $m_{\rm H}$) is used for the mean particle mass in the static initial model which results from a hydrogen to helium number abundance ratio of 10:1 and the assumption that the available hydrogen is in atoms. The abundances of the LMC and SMC lead to a value of $\mu = 1.24$ and 1.23, respectively, which was used in the generation of the initial static atmosphere.

2.2.6 Radiative transfer and optical depth

As mentioned earlier, the approximate treatment of the radiative transfer in the circumstellar shell is reconsidered for less than solar metallicity.

The extinction coefficient $\chi_F = \chi_F^{\rm d} + \chi_F^{\rm g}$ has contributions due to the gas and the dust. To calculate the dust opacity the flux-mean extinction coefficient $\chi_F^{\rm d}$ is approximated by the Planck-mean value $\kappa_P^{\rm d}$ which is given by

$$\kappa_P^{\rm d} = \int \pi a^3 \left(\frac{Q}{a}\right)_P^{\rm abs} f(a) da = \pi a_0^3 Q_P'^{\rm abs} K_3 \tag{2.18}$$

That is to say, the dust extinction $\chi^{\rm d}$ is calculated in the small particle limit neglecting scattering and is given by the third moment of the dust distribution function $f(a)$ and tabulated (temperature dependent) extinction efficiencies $Q_P'^{\rm abs}(T)$. For the latter we use values for amorphous carbon grains by Preibisch et al. (1993).

type	$L_\star$ [$L_\odot$]	$T_\star$ [K]	$M_\star$ [$M_\odot$]	ϵ_C/ϵ_O	P [d]	Δv [km/s]
LMC	5000 . . . 15000	2200 . . . 3200	0.7 . . . 1.0	1.3/1.8	325 . . . 650	2/5
SMC	7000 . . . 12000	2400 . . . 3000	0.6 . . . 1.1	1.8	450 . . . 650	5

Table 2.2: Essential input parameter ranges covered by our collection of subsolar metallicity models.

In the solar case the shell has been considered to be optically thick so that the flux-averaged dust extinction is determined by the local equilibrium radiation field. However, if the atmosphere is considered to be partly transparent, the dust grains are to some extent exposed to the direct radiation from the stellar photosphere. Therefore, the flux-mean dust opacity is for lower metallicity represented by assuming a non-local radiation field, which is characterised by the temperature T and determined according to

$$T^4 = T_\star^4 e^{-\tau} + T_{\rm eq}^4 (1 - e^{-\tau}) \tag{2.19}$$

i.e. the radiation field is interpolated in optical depth τ between the local equilibrium radiation and the stellar (black-body) radiation field (represented by $T_\star$ and $T_{\rm eq}$, respectively).

The gas opacity $\kappa_{\rm g}/\rho$ is set to a constant value of 2×10^{-4} cm^2 g^{-1} in the solar models. From figure 2 of Helling et al. (2000) it is clear that the mean opacity drops with lower metallicity. Therefore, we reduced the value of the gas opacity in the LMC and SMC models to 1×10^{-4}, and 0.5×10^{-4} cm^2 g^{-1}, respectively.

2.3 Results

Some 200 models have been calculated with the new version of the code. Since the main purpose of this work is to derive mass-loss rates for subsolar metallicities, the focus when choosing the model parameters was primarily on covering the range of stellar parameters M, L, and T provided by the stellar evolution code for each fixed element composition (LMC/SMC) than on performing a detailed parameter study. In section 2.3.4 the dependence on the carbon overabundance is shortly discussed, though. Table 2.2 summarises the parameter ranges of our low metallicity model sets. The complete collection of models can be found in appendix A. Table A.1 lists models with LMC element abundances, and table A.2 those with SMC abundances. Columns 1–6 contain the model parameters. An explanation of columns 7–11 is given in section 2.3.2.

2.3.1 Radial structure

Before introducing and discussing averages of radius dependent quantities, the radial structure of different models is presented. Basically, there exist two distinct types of models:

a) models where effective dust formation and growth is taking place, finally leading to a radiative acceleration on the dust grains which is sufficient to drive a stable wind, and b) those showing a flat, "quasi-stationary" nature where not enough dust is formed to dominate the hydrodynamic structure of the wind. For solar element abundances this has been discussed in detail by Winters et al. (2000).

Figure 2.2 shows typical examples of each type with SMC abundances. The models shown here only differ in luminosity.

The model with the higher luminosity, figure 2.2(a), clearly shows a layered structure. Firstly, there are dust shells present which are represented by the peaks of the dust density $n_{\rm d}$. Furthermore, the degree of condensation $f_{\rm c}$ (giving the fraction of condensable material which is condensed into dust grains) almost reaches unity in several regions. Those peaks are visible as well in the acceleration curve. The velocity structure is marked by shock waves propagating outwards. Generally this type of models shows high mass-loss rates.

As can be seen in figure 2.2(b), the other type instead shows an overall smooth structure. There are no pronounced peaks in any of the above mentioned quantities. Therefore in this type of models shock fronts do not develop and dust shells are not present.

2.3.2 Resulting averaged quantities

In order to characterise the outflow of each time dependent wind model time-averages of several quantities are calculated. The most obvious quantities for this purpose are the mass-loss rate $\langle \dot{M} \rangle$ and the final outflow velocity $\langle v_\infty \rangle$. Furthermore we consider the dust-to-gas ratio $\langle \rho_{\rm d}/\rho_{\rm g} \rangle$ and the ratio of radiative to gravitational acceleration $\langle \alpha \rangle$, since these are expected to be significant for the general behaviour of the wind.

Having a look at the radial structure of, e.g., the final outflow velocity of a model one can see that at a certain instant of time it is best described by a radial average over the outermost radii since there still are dampened remnants of the shock waves present. Therefore we first average $\dot{M}$, v, and $\rho_{\rm d/g}$ in the radial coordinate between 40 and 60 $R_\star$ and then over time, typically 20 periods for LMC and 80 periods for SMC models. For $\langle \alpha \rangle$ a different procedure is followed, though. It is the average of the ratio of radiative to gravitational acceleration at the radius of the first maximum of the condensation degree, i.e. the innermost dust shell, and therefore a time-average only. One could of course imagine other definitions of the α mean, for instance taking it at the critical point[3], but the one used here characterised the outflow well.

Typical variations of the derived quantities which occur when choosing different periods for averaging are illustrated by two examples in table 2.3. In most cases the resulting values

[3]The critical point is defined to be the radius where the outflow velocity equals the sound speed. In a shocked atmosphere it might not be uniquely defined, though. See for example figure 2.2(a) where the conditions is fulfilled at three radii.

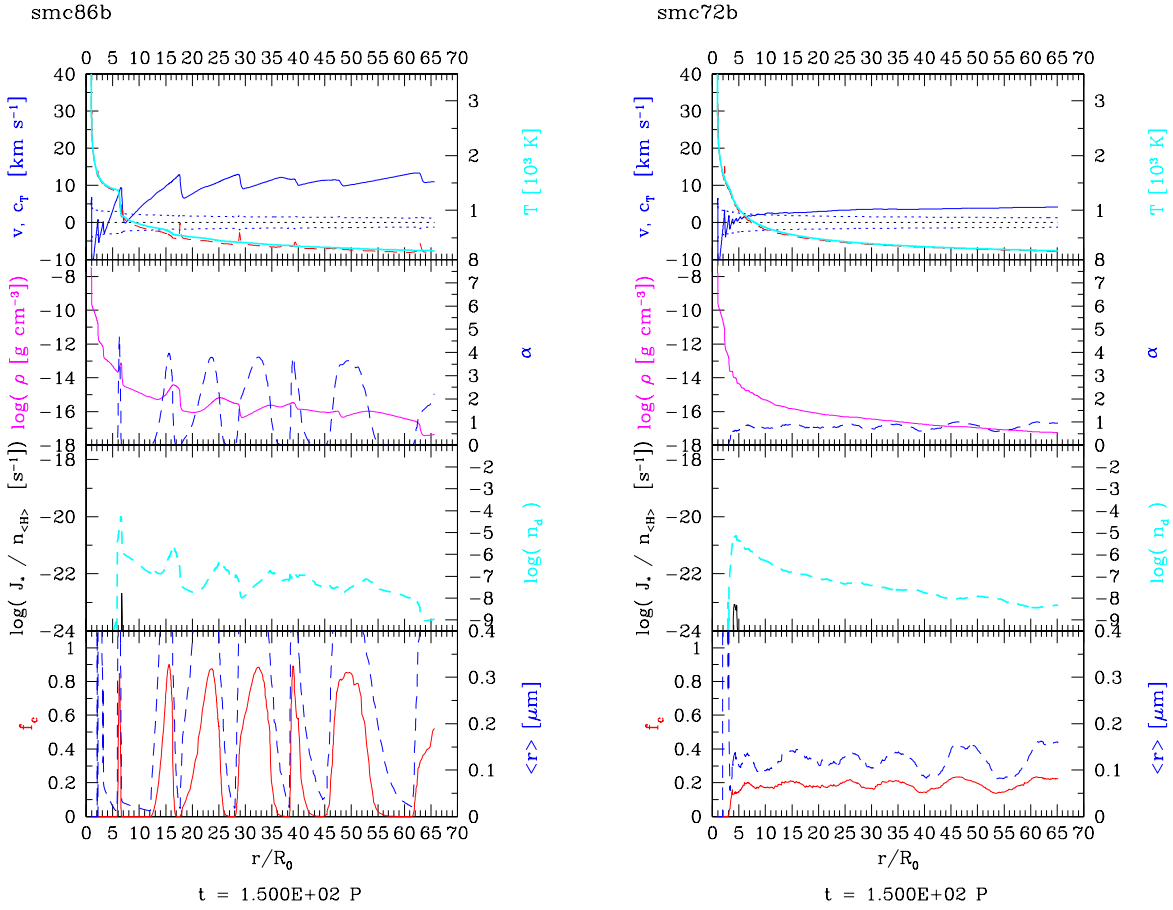

(a) $L_\star = 12000\ L_\odot$ (b) $L_\star = 9000\ L_\odot$

Figure 2.2: Radial structure of SMC models. Input parameters: $T_\star = 3000$ K, $M = 0.8\ M_\odot$, $P = 700$ d, $\Delta v = 5$ km s^{-1}, $\epsilon_\mathrm{C}/\epsilon_\mathrm{O} = 1.8$. Shown are (left scales) the radial velocity v, the speed of sound c_T, the density ρ of the material, the nucleation rate per hydrogen atom $J_\star/n_{\langle H\rangle}$, and the degree of condensation f_c of the dust, (right scales) the temperature T, and the ratio of radiative to gravitational acceleration α of the material, the dust density n_d, and the mean dust particle radius $\langle r\rangle$.

differ by less than 5%.

2.3.3 Differences due to the modified opacity treatment

Before presenting models with subsolar abundances resulting from the new version of the code the main influences of the modified treatment of the optical depth as described in section 2.2.6 needs to be considered. For this purpose we performed test calculations with both versions using identical input parameters. Their results are summarised in table 2.3.

The acceleration ratio $\langle\alpha\rangle$ as well as the final outflow velocity v_∞ are increased by typically a factor of 2, while the average dust-to-gas ratio $\rho_{\mathrm{d/g}}$ is virtually unaffected and slightly decreased respectively.

The mass loss rate $|\dot{M}|$ averaged over the given period range is not influenced within accuracy by this modification[4]. The ratios are very similar to the ones resulting when using different periods for the average. The latter variations occur since the models do not exactly have the same structure after each period, some rather show a multiperiodic behaviour (see Fleischer 1994).

2.3.4 Influence of the C/O ratio

The C/O abundance ratio determines how much carbon is available for dust formation, since we consider carbon rich chemistry and total CO-blocking. As far as the derivation of a mass loss formula applicable for stellar evolution is concerned, the solar models already demonstrated that the mass loss rate does not depend heavily on this model parameter (see Arndt et al. 1997; Wachter et al. 2002). Instead it can be seen as a critical parameter in the sense that the mass loss rate remains the same order of magnitude once the C/O ratio is above a certain threshold.

Some test calculations for LMC and SMC abundances with varying C/O ratio are summarised in table 2.4[5]. In the LMC models with $\epsilon_{\mathrm{C/O}} = 1.3$ and 1.5 the material expands so slowly that after 110 and 90 periods the outermost grid point has just reached 10 and 25 stellar radii, respectively. This is well below the region of 40 to 60 stellar radii where we generally take the averages. The calculations have not been followed any further since the models up to that period show a virtually stationary radial structure.

2.3.5 Comparison of models with different element abundances

As pointed out earlier, the main aspect of this work is to consider mass loss at subsolar metallicities. Thereby we focus on element abundances as found in the Magellanic Clouds.

[4] As it happens this quantity is the most relevant quantity for our study.

[5] Values $\epsilon_{\mathrm{C/O}} > 2.5$ are not considered, since they are unrealistically high.

M	T	L	$\epsilon_{\mathrm{C/O}}$	P	Δv	type	periods	$\lvert\dot{M}\rvert$	α	v_∞	$\rho_{\mathrm{d/g}}$
0.80	3000	6000	1.30	400	5.00	org	90–130	4.41e-06	1.74	8.99	8.37e-4
0.80	3000	6000	1.30	400	5.00	new	90–130	3.99e-06	4.07	20.36	8.49e-4
							ratio new/org:	0.90	2.34	2.27	1.01
0.80	3000	6000	1.30	400	5.00	org	130–150	4.26e-06	1.91	9.57	8.78e-4
0.80	3000	6000	1.30	400	5.00	new	130–150	4.20e-06	4.18	20.59	8.14e-4
							ratio new/org:	0.99	2.19	2.15	0.93
							ratio org (90–130)/(130–150):	1.04	0.91	0.94	0.95
							ratio new (90–130)/(130–150):	0.95	0.97	0.99	1.04
1.00	2600	3500	1.80	650	2.00	org	91–130	4.14e-07	2.57	21.34	3.26e-3
1.00	2600	3500	1.80	650	2.00	new	91–130	4.12e-07	4.48	40.76	2.61e-3
							ratio new/org:	1.00	1.74	1.91	0.80
1.00	2600	3500	1.80	650	2.00	org	130–150	3.84e-07	2.48	20.96	3.15e-3
1.00	2600	3500	1.80	650	2.00	new	130–150	4.71e-07	4.38	40.32	2.66e-3
							ratio new/org:	1.23	1.77	1.92	0.84
							ratio org (91–130)/(130–150):	1.08	1.04	1.02	1.03
							ratio new (91–130)/(130–150):	0.87	1.02	1.01	0.98
1.00	2600	10000	1.80	650	2.00	org	130–150	9.87e-06	6.40	33.88	3.93e-3
1.00	2600	10000	1.80	650	2.00	new	130–150	7.66e-06	8.56	49.83	3.50e-3
							ratio new/org:	0.78	1.34	1.47	0.89

Table 2.3: Comparison between new and old(=org) solar abundance models. Units are $M[M_\odot]$, T[K], $L[L_\odot]$, P[d], Δv[km s^{-1}], $|\dot{M}|[M_\odot$ yr$^{-1}]$, and v_∞[km s^{-1}]. Columns 1–6 give the input parameters, 8–11 the derived averaged quantities. See section 2.3.3 for further explanation.

	$\epsilon_{C/O}$	periods	$\lvert\dot{M}\rvert$	$\langle\alpha\rangle$	v_∞	$\rho_{d/g}$	type
	$M = 0.8\,M_\odot$, $T = 2800$ K, $L = 15000\,L_\odot$, $P = 400$ d, $\Delta v = 5$ km s^{-1}						
	1.30	Expansion after 110 P: < 10 R$_\star$					
	1.50	Expansion after 90 P: < 25 R$_\star$					
	1.70	70–90	3.51e-05	6.10	18.83	2.01e-3	LMC
	1.80	70–90	3.30e-05	3.92	21.04	2.68e-3	
	2.50	70–90	4.58e-05	6.03	30.16	7.13e-3	
	$M = 1.0\,M_\odot$, $T = 2600$ K, $L = 11000\,L_\odot$, $P = 650$ d, $\Delta v = 5$ km s^{-1}						
	1.30	70–150	—	—	—	—	
$\alpha < 1$	1.50	70–150	7.17e-07	0.06	3.23	1.69e-4	
	1.70	70–150	4.74e-06	0.11	4.95	1.17e-3	SMC
$\alpha > 1$	1.80	70–150	3.69e-05	1.26	8.56	1.82e-3	
	2.00	70–150	4.55e-05	2.19	10.61	2.75e-3	
	$M = 0.8\,M_\odot$, $T = 2800$ K, $L = 10000\,L_\odot$, $P = 600$ d, $\Delta v = 5$ km s^{-1}						
$\alpha < 1$	1.30	130–150	1.24e-07	0.27	1.91	1.93e-9	
	1.50	70–150	8.90e-07	0.21	3.75	4.74e-4	
	1.70	70–150	1.72e-05	1.02	8.31	1.27e-3	SMC
$\alpha > 1$	1.80	70–150	2.88e-05	2.04	10.57	1.75e-3	
	2.00	70–150	3.76e-05	3.11	12.10	2.89e-3	

Table 2.4: Variation of the carbon overabundance $\epsilon_{C/O}$ for otherwise fixed parameters.

In this section we summarise major differences between models with solar, LMC, and SMC abundances.

Table 2.5 lists sets of models with different element abundances but otherwise identical input parameters. Columns 2–4 again contain the resulting averaged quantities of the outflow (as defined in section 2.3.2). In lines 4 and 5 of each set these are normalised to the corresponding solar abundance models.

Generally, when comparing the MC models to the solar ones one finds lower final outflow velocities and lower dust-to-gas ratios. The radiative (in terms of the gravitational) acceleration is weaker as well. For the mass-loss rate though, there are input parameters where the MC models show higher values than the corresponding solar ones.

Typically the outflow velocities of the solar models are higher by about a factor of $2.2(\pm0.2)$ than those of the LMC, and $4(\pm1)$ than those of the SMC. The dust-to-gas ratios are higher by about a factor of $1.3(\pm0.1)$ and $2.3(\pm0.2)$, respectively. For the acceleration the trend is less clear, i.e. the data show a wider spread, especially in the SMC case. Leaving out the most extreme (SMC) values of 50 and 20, the solar abundance models produce values higher by a factor of $3.6(\pm1.2)$, and $5.8(\pm1.2)$, respectively.

Figure 2.3 depicts the radial structure of model $M = 0.9M_{\odot}$, $T_{\star} = 2800$ K, $L = 10^4 L_{\odot}$, $P = 600$ d, $\Delta v = 5$ km s^{-1}, $\epsilon_{\rm C}/\epsilon_{\rm O} = 1.8$ for solar, LMC, and SMC abundances at the instant of 90 periods after starting the model calculation. It gives a good representation of these trends, especially for the outflow velocity and the dust density, recalling that they are not only time but as well radial averages. The acceleration trend is more indirectly represented, since the graph is a time snapshot, but the acceleration average is a time average of the value at the radius of the first maximum of the condensation degree.

In the lowest panels two more trends can be seen. The condensation degree which is closely related to the dust-to-gas ratio by mass

$$\frac{\rho_{\rm d}}{\rho_{\rm g}} = \frac{12}{1.4}\epsilon_{\rm O}(\frac{\epsilon_{\rm C}}{\epsilon_{\rm O}} - 1)f_{\rm c}$$

(see eq. (4.7) of Winters (1994)) is less pronounced and more irregular in LMC and SMC models than in solar models. While in this solar model the condensation degree is virtually 1 in the dust shells, the SMC model only reaches maximum value of about 0.8. I.e. all the condensable material is accumulated in dust grains in the solar model, but with lower metallicity the condensation is less efficient. The second trend resulting from this simple graphical comparison of respective models concerns the average grain size. In the SMC case the grains reach much higher radii than with solar abundances.

$M[M_\odot]$, $T_\star$[K], $L_\star[L_\odot]$, $\epsilon_{\mathrm{C/O}}$, P[d], Δv[km s^{-1}]					
type	$\lvert\dot{M}\rvert$ $[M_\odot \mathrm{yr}^{-1}]$	α	v_∞ [km s^{-1}]	$\rho_{\mathrm{d/g}}$	periods
0.6, 2800, 8000, 1.8, 500, 5					
SMC	3.69e-05	2.53	9.69	1.73e-3	70–150
LMC	5.95e-05	3.22	14.30	3.35e-3	70–150
solar	2.72e-05	10.22	33.20	4.07e-3	70–150
ratio SMC/solar:	1.36	0.25	0.29	0.43	
ratio LMC/solar:	2.19	0.32	0.43	0.82	
0.6, 2800, 10000, 1.8, 600, 5					
SMC	7.18e-05	3.02	9.66	2.03e-3	70–150
LMC	7.09e-05	4.46	17.31	3.41e-3	70–150
solar	4.22e-05	15.44	32.50	4.26e-3	70–150
ratio SMC/solar:	1.70	0.20	0.30	0.48	
ratio LMC/solar:	1.68	0.29	0.53	0.80	
0.6, 3000, 10000, 1.8, 600, 5					
SMC	4.47e-05	3.30	10.76	1.95e-3	70–150
LMC	4.61e-05	4.82	19.91	2.63e-3	70–150
solar	2.98e-05	23.16	36.65	4.07e-3	70–150
ratio SMC/solar:	1.55	0.14	0.29	0.48	
ratio LMC/solar:	1.50	0.21	0.54	0.65	
0.7, 2800, 8000, 1.8, 500, 5					
SMC	2.37e-05	1.87	9.68	1.68e-3	70–150
LMC	3.26e-05	4.01	15.81	3.15e-3	70–150
solar	1.95e-05	10.67	33.71	4.04e-3	70–150
ratio SMC/solar:	1.22	0.18	0.29	0.42	
ratio LMC/solar:	1.67	0.38	0.47	0.78	
0.8, 2400, 10000, 1.8, 600, 5					
SMC	2.19e-05	0.17	5.36	1.87e-3	70–210
LMC	1.03e-05	3.20	14.17	3.58e-3	70–150
solar	5.45e-05	10.50	30.73	4.22e-3	70–150
ratio SMC/solar:	0.40	0.02	0.17	0.44	
ratio LMC/solar:	0.19	0.30	0.46	0.85	
0.8, 2600, 8000, 1.8, 500, 5					
SMC	2.75e-05	1.35	8.33	1.95e-3	70–150
LMC	3.31e-05	2.60	12.94	3.25e-3	70–90
solar	2.38e-05	8.53	32.31	4.12e-3	70–150
ratio SMC/solar:	1.16	0.16	0.26	0.47	
ratio LMC/solar:	1.39	0.30	0.40	0.79	
0.8, 2600, 10000, 1.8, 600, 5					
SMC	5.14e-05	2.11	9.05	1.87e-3	70–150

LMC	8.18e-05	1.85	14.45	3.56e-3	70–90
solar	3.57e-05	12.39	32.91	4.29e-3	70–150
ratio SMC/solar:	1.44	0.17	0.27	0.44	
ratio LMC/solar:	2.29	0.15	0.44	0.83	
0.8, 2800, 10000, 1.8, 600, 5					
SMC	2.88e-05	2.04	10.57	1.75e-3	70–150
LMC	4.58e-05	3.66	16.36	3.27e-3	70–150
solar	2.33e-05	12.45	36.64	3.95e-3	70–90
ratio SMC/solar:	1.24	0.16	0.29	0.44	
ratio LMC/solar:	1.97	0.29	0.45	0.83	
0.8, 2800, 12000, 1.8, 700, 5					
SMC	4.69e-05	2.77	10.75	1.89e-3	70–150
LMC	6.74e-05	3.72	18.04	3.43e-3	70–150
solar	3.23e-05	12.65	37.11	4.07e-3	70–150
ratio SMC/solar:	1.45	0.22	0.29	0.46	
ratio LMC/solar:	2.09	0.29	0.49	0.84	
0.9, 2800, 10000, 1.8, 600, 5					
SMC	1.92e-05	1.36	9.60	1.56e-3	70–150
LMC	3.17e-05	3.23	16.77	2.98e-3	70–90
solar	1.94e-05	10.85	38.78	3.84e-3	70–150
ratio SMC/solar:	0.99	0.13	0.25	0.41	
ratio LMC/solar:	1.63	0.30	0.43	0.78	
1.0, 2600, 10000, 1.8, 600, 5					
SMC	1.19e-05	0.44	5.85	1.41e-3	70–150
LMC	3.81e-05	3.39	15.96	3.46e-3	70–90
solar	2.19e-05	8.26	36.13	4.19e-3	70–90
ratio SMC/solar:	0.54	0.05	0.16	0.34	
ratio LMC/solar:	1.63	0.41	0.44	0.83	

Table 2.5: List of solar, LMC, and SMC wind models with identical input parameters.

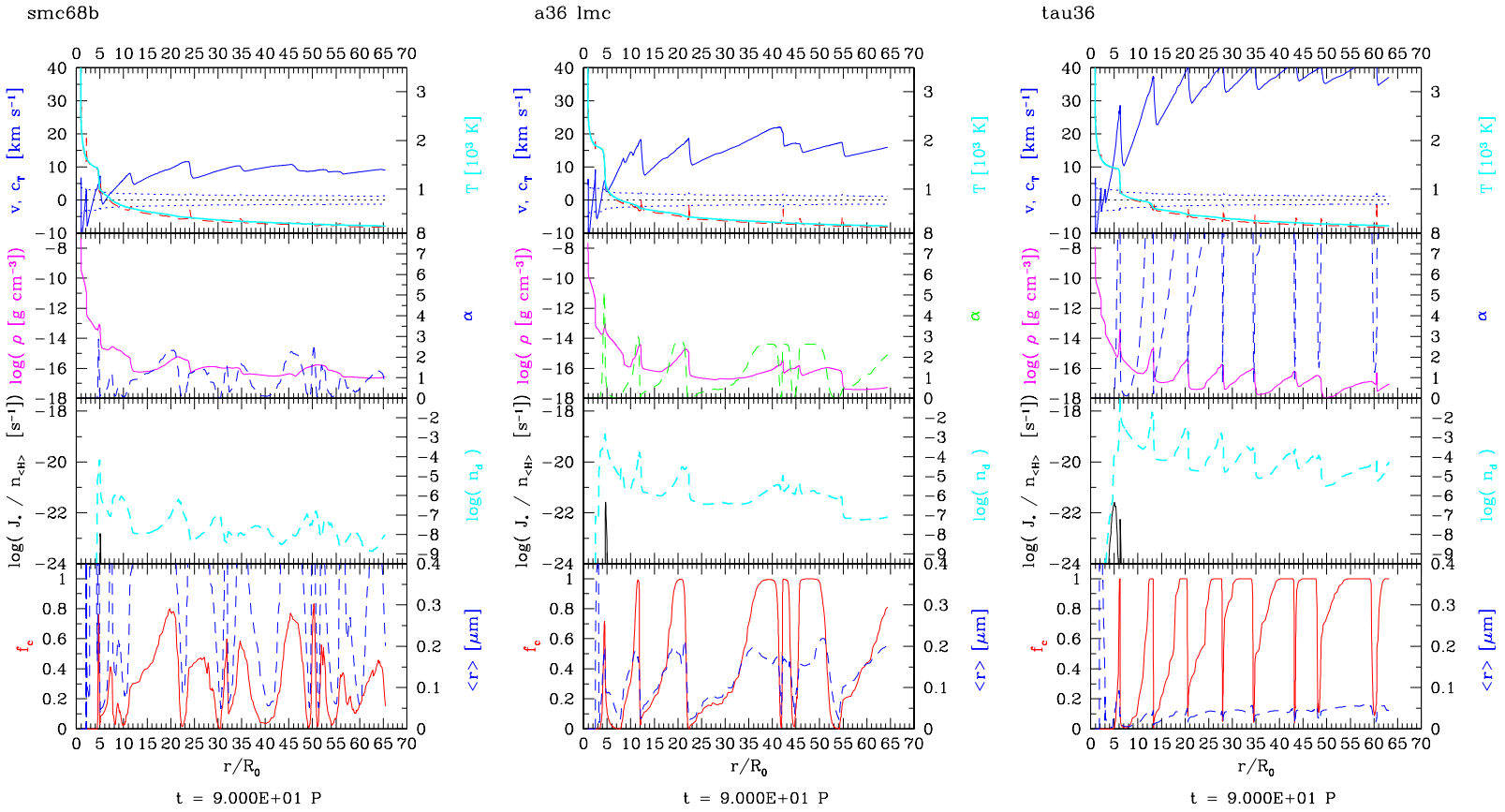

(a) SMC (b) LMC (c) solar

Figure 2.3: SMC, LMC, and solar model with identical input parameters: M=0.9 $M_\odot$, $T_\star$=2800 K, L=$10^4 L_\odot$, P=600 d, Δv = 5 km s^{-1}, ϵ_C/ϵ_O=1.8. Plotted are the same quantities as in figure 2.2.

2.3.6 Model grid

Figure 2.4 gives an overview of all models involved in this study. Plotted are the averaged mass loss rates over the time-averaged ratio of radiative to gravitational acceleration. Figure 2.4(a) shows the values of each LMC model (as listed in table A.1), and 2.4(b) the SMC ones (as given in table A.2). Clearly, high $\langle\alpha\rangle$ values are related to high mass loss rates. Wind models with $\langle\alpha\rangle > 1$ are dust-driven and their radial structure resembles that of figures 2.2(a) and 2.3. The others show less pronounced structural features or are even quasi-static as depicted in figure 2.2(b).

2.4 Resulting mass-loss formulae

Since we are interested in obtaining a mass loss formula for dust-driven winds the whole set of models presented in the previous section 2.3.6 needs to be filtered. As pointed out above the models with a stable wind are characterised by $\langle\alpha\rangle > 1$, i.e. we only take models into account fulfilling this criterion.

Furthermore, the formula should be applicable to stellar evolution and therefore only depend on the stellar parameters luminosity L, effective temperature T, and mass M. Fortunately, the models are most sensitive to these input parameters (already pointed out for solar models by Arndt et al. 1997). For the LMC and SMC models we followed the approach by Wachter et al. (2002) for their revised formula for solar models. Setting the abundance ratio $\epsilon_{\mathrm{C/O}}$ to 1.8 allows for the fact that it has to be high enough to produce a stable wind (see 2.3.4) without being unreasonable (see the discussion in 2.5). As to the velocity amplitude Δv, one of the "mechanical" parameters resulting from the piston approximation for the inner boundary, we consider only values of 5 km s^{-1}, as has been done with the solar models earlier, since models with this value give the best match of observed Mira light curves.

Concerning the period P we relied on observed period-luminosity relations of LPVs. Wachter et al. (2002) took it into account by transferring the slight dependence on the period to an additional luminosity term. In contrast, we now take the period dependence into account more directly by choosing only those models where the P-L relation (extrapolated from Groenewegen & Whitelock 1996) is fulfilled. This is possible since we now have a larger set of models at hand.

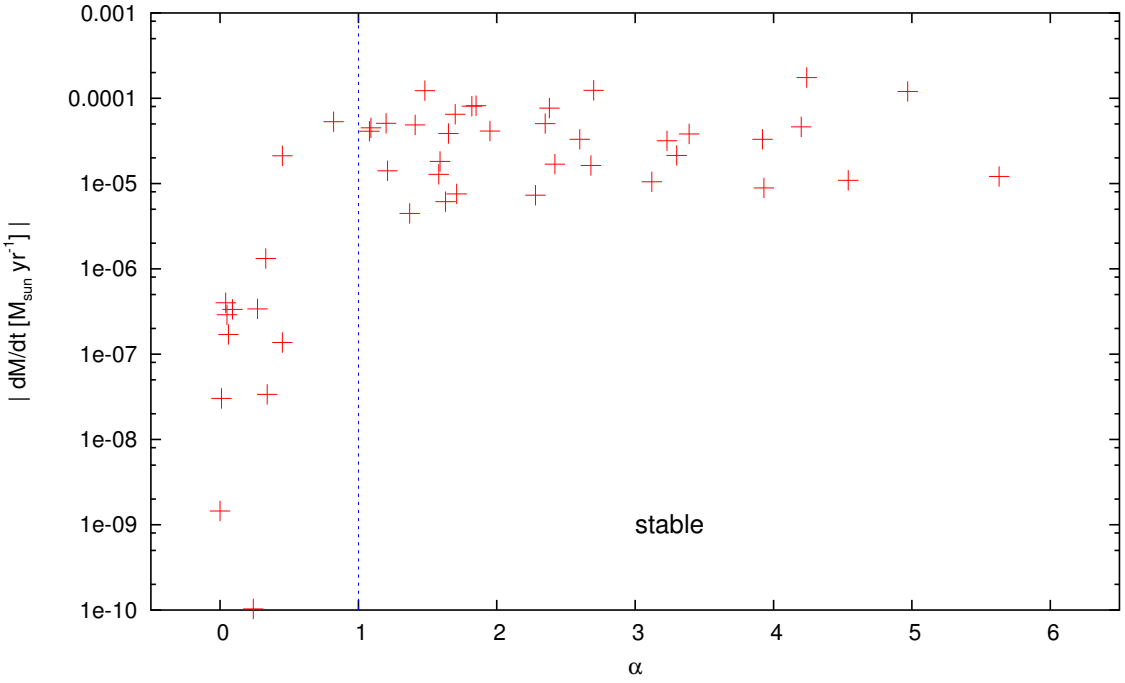

(a) ...for all LMC models

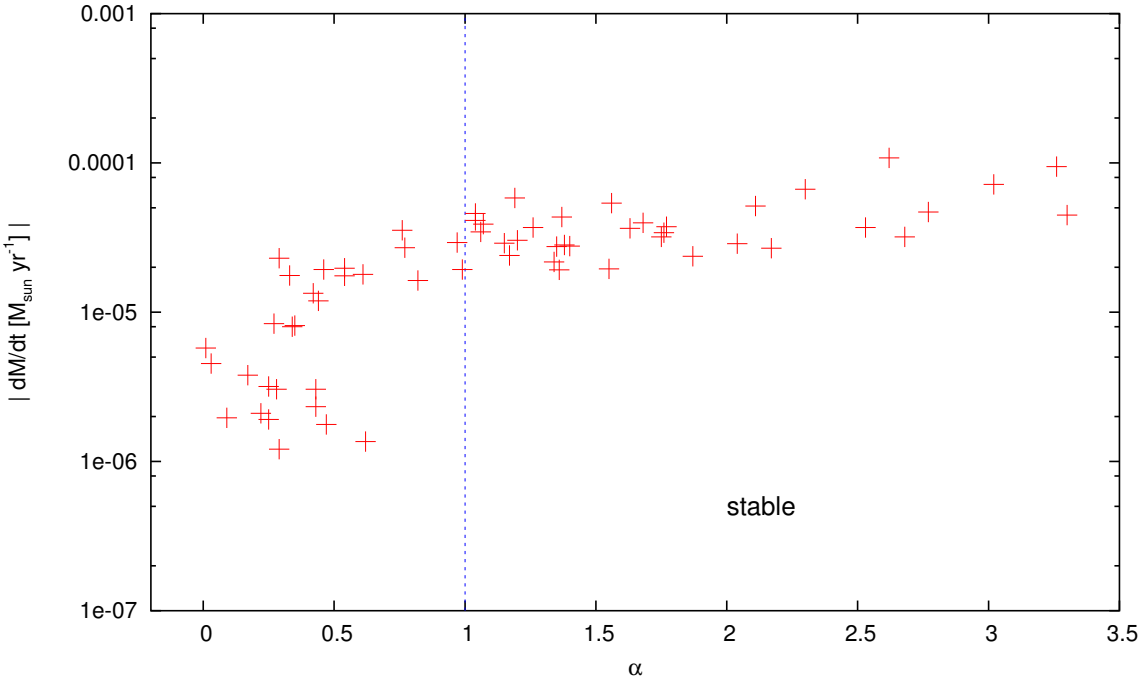

(b) ...for all SMC models

Figure 2.4: Averages of mass loss rate over ratio of radiative to gravitational acceleration... (Attention, axis have different scales!)

2.4.1 Approximative formulae

For the selected LMC models a multi-linear least square fit of the form $\log \dot{M} = a_0 + a_1 * \log x_1 + \ldots$ was performed leading to the following formula:

$$|\dot{M}[M_\odot\,\mathrm{yr}^{-1}]| = 3.80 \times 10^{-5} \times (M_\star[M_\odot])^{-2.56} \times \left(\frac{T_\star[\mathrm{K}]}{2600}\right)^{-7.44} \times \left(\frac{L_\star[L_\odot]}{10^4}\right)^{2.86} \quad (2.20)$$

with a correlation coefficient of $K = 0.98$.

For the SMC models the result is:

$$|\dot{M}[M_\odot\,\mathrm{yr}^{-1}]| = 2.34 \times 10^{-5} \times (M_\star[M_\odot])^{-3.01} \times \left(\frac{T_\star[\mathrm{K}]}{2600}\right)^{-6.22} \times \left(\frac{L_\star[L_\odot]}{10^4}\right)^{2.84} \quad (2.21)$$

with a correlation coefficient of $K = 0.97$.

The formula for solar element composition as published in Wachter et al. (2002) reads, for comparison:

$$|\dot{M}[M_\odot\,\mathrm{yr}^{-1}]| = 4.52 \times 10^{-5} \times (M_\star[M_\odot])^{-1.95} \times \left(\frac{T_\star[\mathrm{K}]}{2600}\right)^{-6.81} \times \left(\frac{L_\star[L_\odot]}{10^4}\right)^{2.47} \quad (2.22)$$

where the correlation coefficient is $K = 0.97$.

As already pointed out for the solar case, the most influential parameter in the formulae for LMC/SMC abundances is again the effective temperature. This reflects the extreme sensitivity of the dust nucleation with respect to the local temperature.

Graphical illustrations of the formulae for LMC and SMC are given in figure 2.5 for a fixed mass of $M_\star = 1.0\,M_\odot$, temperature range of 2400 ... 3000 K, and luminosity of 5000 ... 15000 $L_\odot$. The lines on the base of the diagrams are projections of contour lines, i.e. they mark those temperature and luminosity values for which the resulting mass-loss rate is 10^{-4}, 5×10^{-5}, 10^{-5}, and 5×10^{-6} $M_\odot$ yr^{-1}, respectively. These show that for the SMC higher luminosities / lower temperatures are necessary to reach the same mass loss rate as in the LMC.

2.4.2 Critical luminosity

For application to stellar evolution the criterion $\langle\alpha\rangle > 1$ needs to be expressed in terms of the stellar parameters, since $\langle\alpha\rangle$ is a quantity which does not appear in these evolutionary models. For this purpose figure 2.6 shows for instance the luminosity divided by mass L/M over effective temperature T for all SMC models. Models with an acceleration ratio of less than one are depicted in red, with higher than one in green. The squares mark the transition point for each temperature. These models have been taken into consideration when deriving the critical luminosity. Since models with a temperature of 2400 K do not show a clear behaviour, no transition model has been included at this temperature.

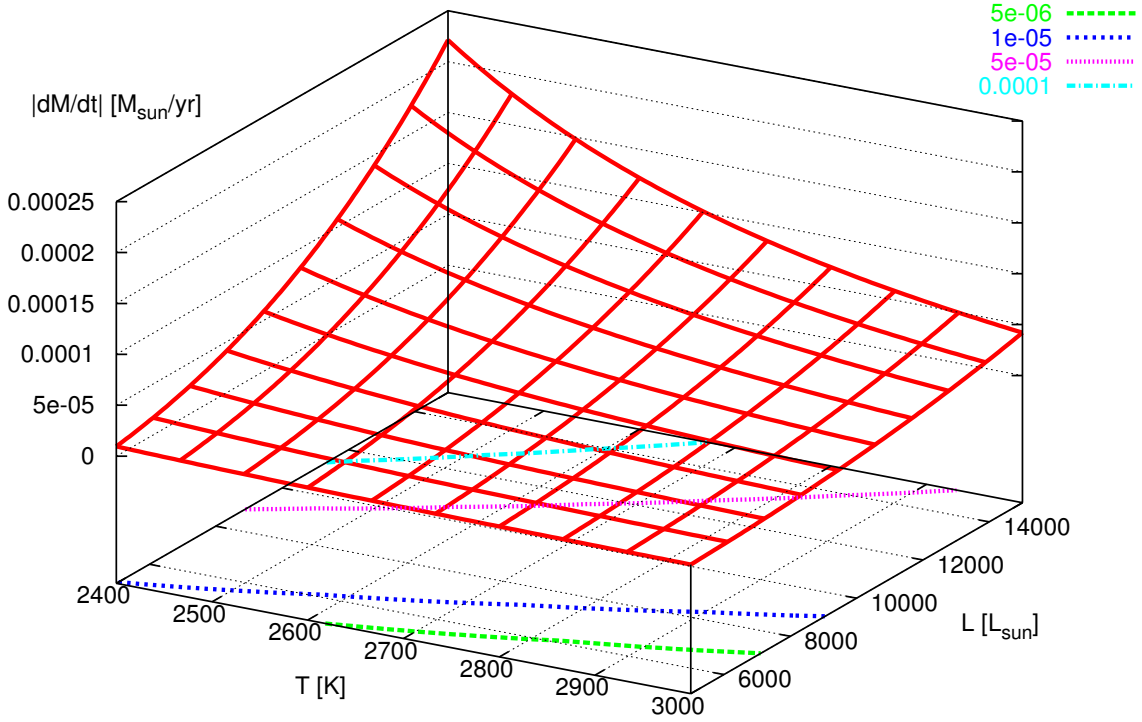

(a) LMC models (equation 2.20)

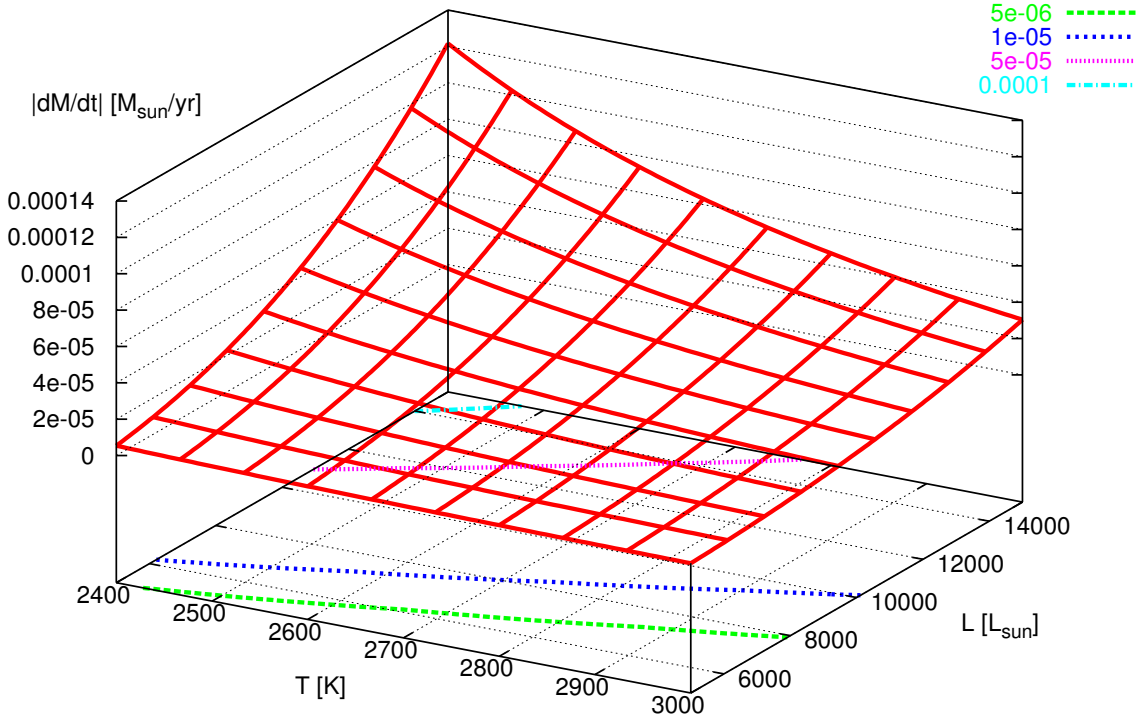

(b) SMC models (equation 2.21)

Figure 2.5: Graphical illustration of the fit formulae for the mass loss rate for fixed mass $M_\star = 1.0\,M_\odot$.

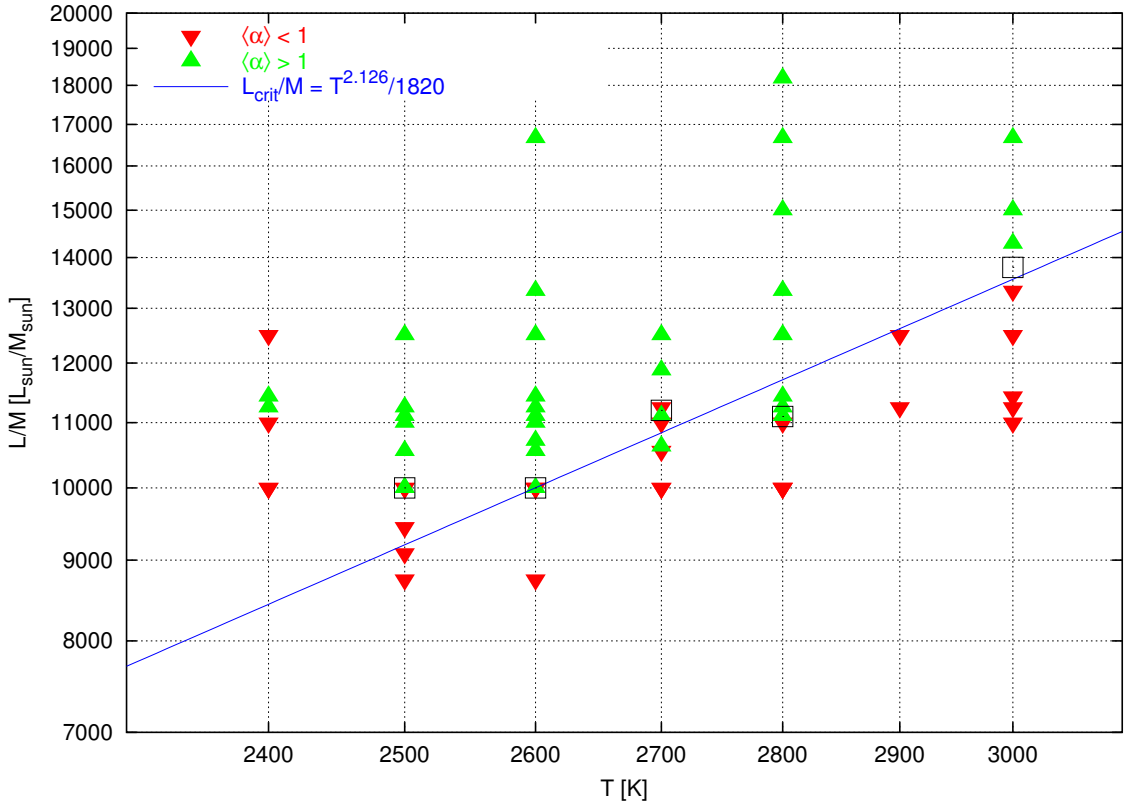

Figure 2.6: SMC models: determination of the critical luminosity (for details see section 2.4.2).

Equations 2.20 and 2.21 are valid for

$$L > L_{\rm crit} \quad , \quad L_{\rm crit} = \begin{cases} 5.58 \times 10^{-8}\, T^{3.198}\, M, & \text{LMC} \\ 5.47 \times 10^{-4}\, T^{2.126}\, M, & \text{SMC} \end{cases} \tag{2.23}$$

2.5 Concluding remarks

As already mentioned, the gas opacity is set to be constant in the calculations. Bowen (1988) chose rather arbitrarily a value of $\kappa = 2 \times 10^{-4}$ cm^2 g^{-1} for solar element abundances to represent the available opacity data in the relevant temperature and density regime. We used the same value for solar element abundances and reduced it to 1×10^{-4} for LMC and 0.5×10^{-4} cm^2 g^{-1} for SMC abundances following figure 2 in Helling et al. (2000).

In order to account for carbon-rich chemistry, we enhance the carbon element abundance considering the C/O ratio as a model parameter. In this work we considered mainly values of 1.3 and 1.8, the latter especially in models with SMC abundances. For most C-stars this value is admittedly rather extreme. Nevertheless, recently Matsuura et al. (2005) reported C/O values derived from theoretical calculations higher than 1.4 for the SMC.

Van Loon et al. (2005) observed AGB stars in the Large Magellanic Cloud, C-stars as well as M-type stars, and derived mass-loss rates of $\log \dot{M}[M_\odot\ \mathrm{yr}^{-1}] \sim$ -5.6 ... -5 for C-type and $\sim$ -5 ... -4.2 for M-type giants. Furthermore, they give an empirical mass-loss formula for these stars dependent on effective temperature and luminosity

$$\log \dot{M}[M_\odot\,\mathrm{yr}^{-1}] = -5.65^{\pm 0.15} + 1.05^{\pm 0.14} \log\left(\frac{L}{10^4 L_\odot}\right) - 6.3^{\pm 1.2} \log\left(\frac{T_{\rm eff}}{3500\,\mathrm{K}}\right)$$

They already compared their formula to equation 2.22 derived from our models with solar abundances (see also Wachter et al. 2002). Even though the dependence of our LMC formula on effective temperature is stronger, it is consistent with their observed value within the errors. Furthermore, they argued that even if their observed luminosity dependence is much lower than our theoretical value, they may still be consistent as the effect of decreasing mass-loss rate with increasing stellar mass counteracts the luminosity dependence.

Chapter 3

Stellar Evolution Calculation

This chapter describes the application of the mass loss formula derived in the previous chapter to stellar evolution. First, the stellar evolution code is briefly presented and details about the mass loss are given. Finally, the results for individual initial masses are presented as well as the collective output of stellar samples.

3.1 Stellar evolution code

For our evolution calculation we use the code originally developed by Eggleton (1971, 1972, 1973). Since then it has seen several updates, of which Han et al. (1994) and Pols et al. (1995) have subsumed the major developments. In the following we give a short summary of the physical ingredients.

3.1.1 Basic equations and assumptions

First of all, spherical symmetry is assumed for the structure as it still is a common approach and stellar rotation is neglected. Under these assumptions the stellar structure equations read:

$$\frac{dm}{dr} = 4\pi r^2 \rho \tag{3.1}$$

$$\frac{dP}{dr} = -\rho G \frac{m}{r^2} \tag{3.2}$$

$$\frac{dl}{dr} = 4\pi r^2 \rho \epsilon \tag{3.3}$$

$$\frac{dT}{dr} = \begin{cases} -\frac{3}{16\sigma}\frac{\kappa\rho}{T^3}\frac{l(r)}{4\pi r^2} & \text{radiation} \\ (1-\frac{1}{\gamma})\frac{T}{P}\frac{dP}{dr} & \text{convection} \end{cases} \tag{3.4}$$

with r is radius, $m(r)$ the mass enclosed in a sphere with radius r, ρ local density, P pressure, T temperature, l luminosity, ϵ energy production rate per unit mass, κ opacity,

and $\gamma = c_P/c_V$ is the ratio of the heat capacities.

As elaborated by Eggleton (1972, 1983) the equations for composition include mixing by convection by assuming a diffusion-type form:

$$\frac{\partial}{\partial r}(D\frac{\partial X_i}{\partial r}) = \frac{d\,X_i}{d\,t} + \sum_j R_{ij} \tag{3.5}$$

where X_i denotes the abundance of the i-th element (see section 3.1.2), and R_{ij} the rates of all reactions which consume or produce this element. This means that the code treats convective mixing as a diffusion process. The diffusion constant D is assumed as a function of the difference between the radiative and the adiabatic temperature gradient ($\nabla_{\rm rad} - \nabla_{\rm ad}$). For the description of the heat transport, though, the code employs the mixing-length theory.

For solving the equations a non-Lagrangian mesh is used, where the mesh points are distributed on equal intervals of a mesh-spacing function Q which is chosen to depend on P, T, m, and r allowing it to cover, e.g. shell burning zones with significantly fewer mesh points, which makes this code economical to run.

The structure equations, supplemented by the equations for the composition and the mesh-point distribution, are discretised as described in Eggleton (1971) using a central-difference scheme. At each time step all equations are solved simultaneously using an implicit Newton-Raphson procedure.

The calculations are started from a homogeneous main sequence model with a fixed number of 199 mesh points. The initial hydrogen and helium abundances are chosen to depend on the metallicity according to $X = 0.76 - 3Z$ and $Y = 0.24 + 2Z$ following Pols et al. (1998).

3.1.2 Input data

Nuclear reactions

In the present version the abundances of 5 elements are considered explicitly, namely ^{1}H, ^{4}He, ^{12}C, ^{16}O, and ^{20}Ne, by including a nuclear reaction network of 20 reaction as listed in table 1 of Pols et al. (1995). Other species (like ^{3}He and ^{7}Be) are followed indirectly, since later reactions of a chain of reactions (as for example the pp-cycle) are considered to be in transient equilibrium with the first. The reaction rates are taken from Caughlan & Fowler (1988), supplemented with data from Caughlan et al. (1985). Values for neutrino loss rates are from a series of papers by Itoh et al. (1989, 1992).

Equation of state (EOS)

The equation of state used was derived by Pols et al. (1995) and is an update of the original EOS by Eggleton (1973). It includes partial ionisation (of H and He, other elements are assumed to be fully ionised) and dissociation (of molecular hydrogen), Coulomb interactions between electrons and ions, and pressure ionisation.

Opacities

Tables of radiative opacity which are needed to calculate the temperature stratification are compilated from OPAL data by Rogers & Iglesias (1993) and Alexander & Ferguson (1994) for lower temperatures where molecules are significant.

(Core) Overshooting

The regions where convective mixing takes place are usually determined by means of the Schwarzschild criterion ($\nabla_{\rm rad} - \nabla_{\rm ad} > 0$). Nevertheless there is no actual mechanism stopping the convection elements at this border so that they reach places beyond, which is called overshooting. As pointed out by Schröder & Eggleton (1996) core overshooting influences the evolutionary timescales. The time of hydrogen burning, i.e. the time spent on the main sequence, for instance prolongs when overshooting is taken into account. Often an overshooting length in units of the pressure scaleheight is introduced in order to parameterise this phenomenon. In our evolution code overshooting is considered by a modification of the instability criterion itself using $\nabla_{\rm rad} > \nabla_{\rm ad} - \delta$ to characterise regions with convective mixing with δ being a function of the ratio x between the radiation pressure and the gas pressure $\delta = \delta_{\rm ov}/(2.5 + 20x + 16x^2)$.

3.1.3 Mass loss

Mass loss is included by reducing the stellar mass at the outer boundary. The particular formulation depends on the evolutionary stage. On the main sequence mass loss is neglected, as stars show mass-loss rates of the order of only $\approx 10^{-14}\ M_\odot\ {\rm yr}^{-1}$ as the solar wind. Mass loss is included after the star runs out of hydrogen in the core and reaches the RGB.

For the models with solar metallicity presented in Wachter et al. (2002) we had used the well known Reimers formula (Reimers 1975) which was derived for K giants in our galaxy using dimensional arguments. In order to apply this formula with different metal abundances it would have to be recalibrated, since it contains a tunable parameter which might be different for non-solar metallicities. Schröder & Cuntz (2005) have reconsidered this formula by using theoretically motivated arguments. As a result it now includes two

new terms containing a dependence on the effective temperature and the surface gravity, respectively. They tested and calibrated the formula with the help of several globular clusters and found a fixed value for the parameter which matches all considered metallicities.

The formulae derived in section 2.4.1 are valid above the respective critical luminosities (see section 2.4.2). These are reached when the star has developed up to the tip of the AGB and has entered the thermally pulsing phase.

Around $L_{\rm crit}$ a short transition zone is introduced where the code interpolates between the modified Reimers and the formula based on dust-driven wind models to avoid artificial jumps in the mass-loss rate.

Generally, it can be said that the stars with higher initial mass on the main sequence evolve faster through the RGB phase and spend (respective to their life-time) more time on the AGB. Therefore, the choice of which formula to use when the star is on the AGB has more influence on the evolution the higher the initial stellar main sequence mass.

3.2 Resulting models

In the following we present results obtained when evolving different initial masses from the main sequence on. We have generated model grids with a metallicity of $Z = 0.01$ and $Z = 0.001$ to represent LMC and SMC stars, respectively (see comments in section 3.4). A list of initial masses of the grids are given in table 3.1 where additionally the total mass-loss results (cf. section 3.3) are summarised. As a reminder, for each metallicity grid we use a mass-loss formula based on wind models calculated with individual abundances as found in the LMC / SMC (see section 2.2.5). Within each grid we calculated evolutionary tracks without and with overshooting. When taken into account, the overshoot parameter $\delta_{\rm ov}$ (see section 3.1.2) was set to the value of 0.12, as it has been tested for the stellar evolution code used in this work by Schröder et al. (1997).

3.2.1 Evolutionary tracks

Exemplary evolutionary tracks (luminosity over effective temperature) for each metallicity grid are depicted in figure 3.1, $Z = 0.01$ in the upper, and $Z = 0.001$ in the lower diagram. To allow for a direct comparison both graphs have the same scales. In that way the shift of the main sequence to higher effective temperature due to lower metallicity can clearly be seen. For the element abundances presented here it amounts to about 0.07 dex.

Furthermore, the stars with $Z = 0.001$ reach higher luminosities (up to 0.2 dex) at the tip of the AGB than their $Z = 0.01$ counterparts with same initial mass. This is of importance since at the same time the wind models predict higher critical luminosities (for a dust-driven wind to develop) for SMC abundances than for the LMC, e.g. a factor of 1.7

(a) Z=0.01: Tracks marked with $M = 1.04/1.01$ (green), $M = 1.71/1.62$ (orange/purple), $M = 2.12$ (blue), and $M = 2.90$ (red) are continuations of tracks for initial masses M_i = 1.2, 1.75, 2.25, and 3.0 $M_\odot$, respectively.

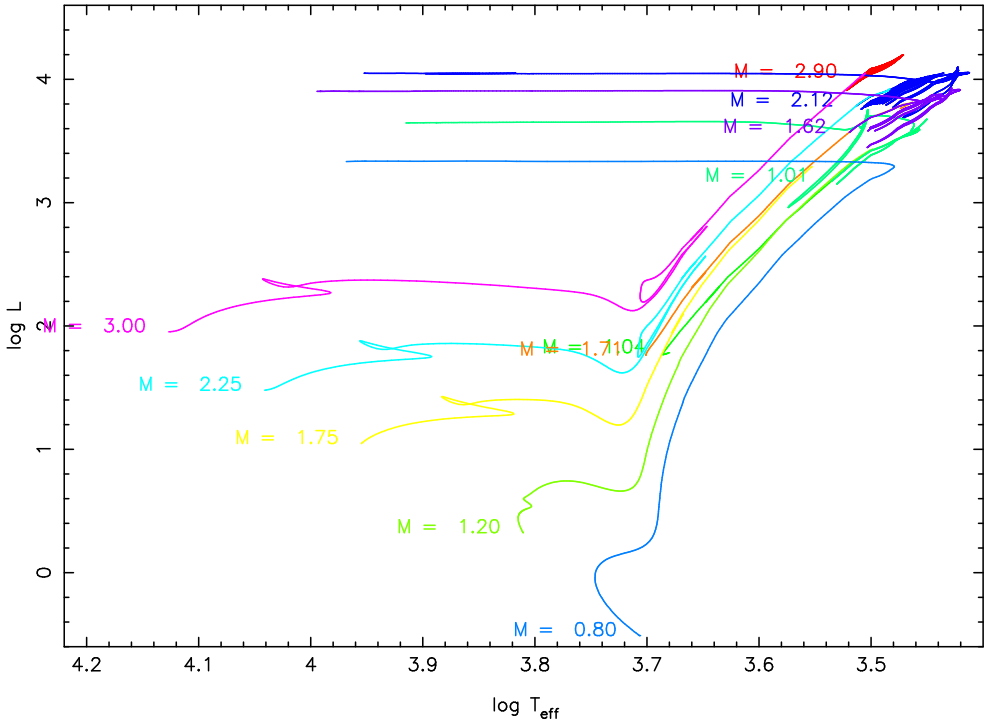

(b) Z=0.001: Tracks marked with $M = 1.09/1.06$ (green), $M = 1.74/1.71$ (orange/purple), $M = 2.17$ (blue), and $M = 2.87$ (red) are continuations of tracks for initial masses M_i = 1.2, 1.75, 2.25, and 3.0 $M_\odot$, respectively.

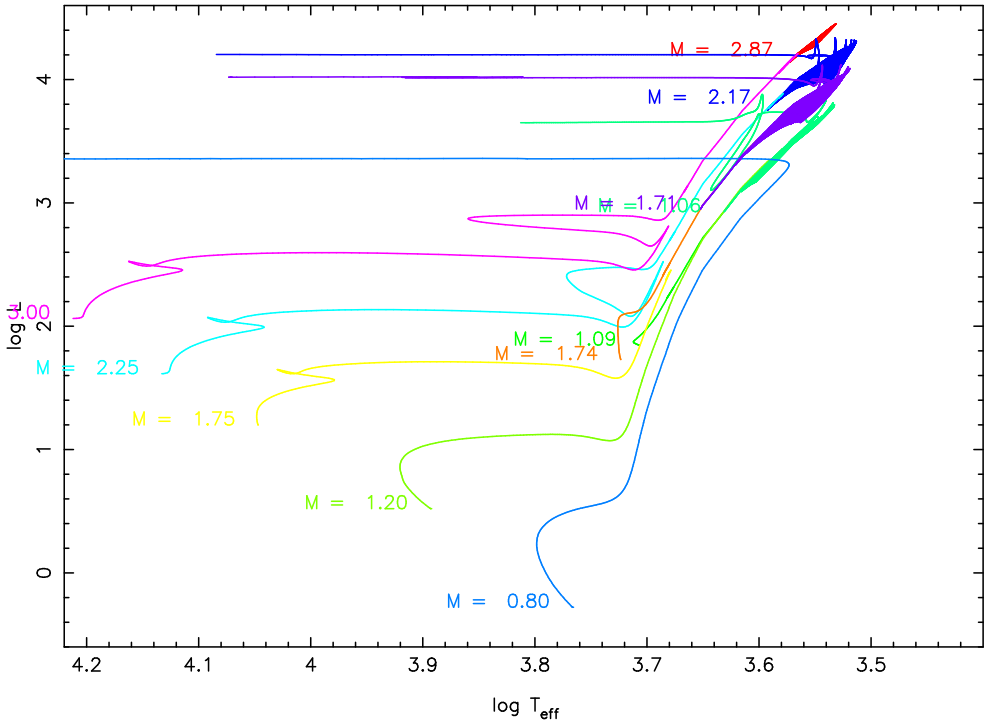

Figure 3.1: Evolutionary tracks for initial masses $M_\mathrm{i} = 0.8$, 1.2, 1.75, 2.25, and 3.0 $M_\odot$. See section 3.2.1 for further explanation.

at $\log T = 3.5$. In other words our models predict SMC stars to undergo mass loss due to dust-driven winds, at least those with initial masses of about two solar masses and higher, despite the higher critical luminosity required to do so.

3.2.2 Mass loss histories

In additional to the total amount of mass a star returns to its surroundings, the temporal development of the stellar mass loss rate is of particular interest. The density structure of a Planetary Nebula is determined by the mass-loss history of its progenitor star.

Figure 3.2 shows four examples of mass-loss rate histories. Depicted are the rates of $Z = 0.01$ models with an initial mass of (a) $M_\mathrm{i} = 1.25\,M_\odot$ and (c) $M_\mathrm{i} = 2.50\,M_\odot$, and $Z = 0.001\,M_\odot$ models with (b) $M_\mathrm{i} = 1.95\,M_\odot$ and (d) $M_\mathrm{i} = 2.50\,M_\odot$. Each graph is plotted over the final 200 000 years of the stellar life, but the scales of the mass-loss rates differ! The graphs (a) and (b) show the results for the lowest initial mass where the critical luminosity is reached and a brief onset of a dust-driven wind results, respectively, while graphs (c) and (d) show the highest initial mass where the evolution is followed until the star leaves the AGB[1].

What catches the eye at first glance is the fact that the number of thermal pulses increases and the inter-pulse duration decreases with decreasing metallicity (cf. figures (c) and (d)). This finding is in accordance with the predictions of other stellar evolution calculations using different mass loss prescriptions, see for example Marigo (2001), and references therein. As pointed out there the exact number of thermal pulses depends on the chosen mass-loss formalism.

Another clear difference is the overall shape of the curve. The $Z = 0.01$ graph resembles the mass-loss rates of our models with solar metallicity, see figures 2–5 in Wachter et al. (2002). For these metallicities the critical luminosities are fairly similar and the stars reside in a regime above that value while they are in the thermally pulsing AGB phase. As a result the mass loss in this late evolutionary stage is controlled by our formula based on dust-driven winds. The $Z = 0.001, M = 2.5\,M_\odot$ rate though is dominated by the modified Reimers law. Only during the last couple of thermal pulses does the star reach luminosities high enough for the dust-driven wind formula to apply. Our present models for SMC-like metallicity therefore result in a rather smooth and broad density distribution of the blown-out material developing to a planetary nebula[2]. Models with solar and LMC abundances though have distinctly higher mass-loss rates during the last $\sim$25 000 years leading to a

[1] The code does not always run through thermal pulses smoothly, typically it breaks down at the start of a thermal pulse when the luminosity drops. Starting from a couple of models before and varying the next time step by hand often (but not necessarily) helps, but is obviously a rather cumbersome procedure.

[2] Naturally, this is a simplified picture, since it disregards different velocities with which the material might be driven away.

(a) $Z = 0.01$, $M_\mathrm{i} = 1.25\,M_\odot$:

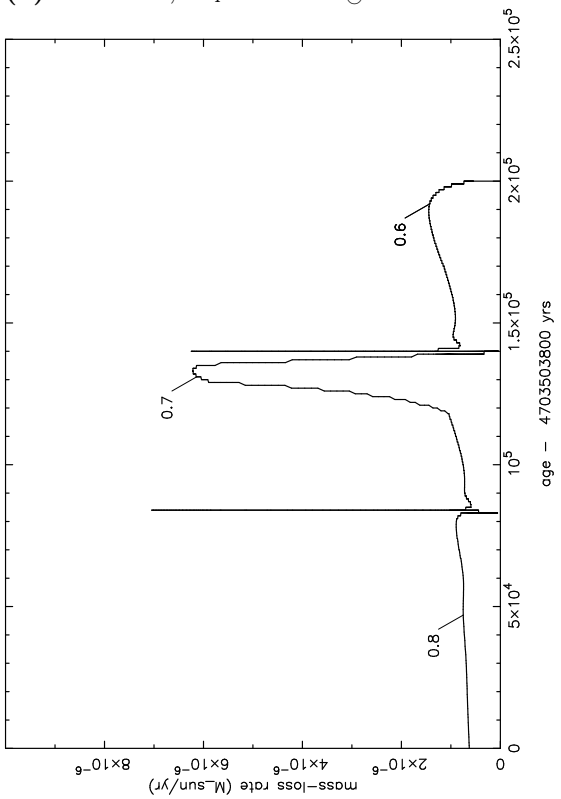

(b) $Z = 0.001$, $M_\mathrm{i} = 1.95\,M_\odot$:

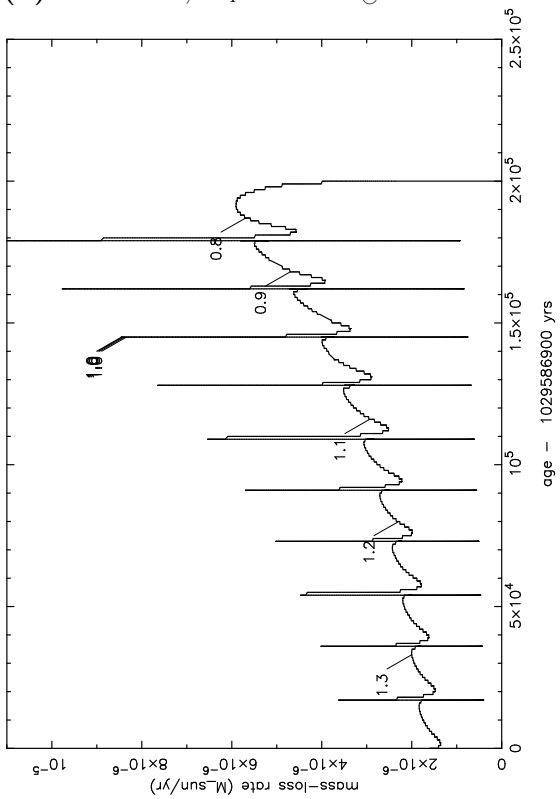

(c) $Z = 0.01$, $M_\mathrm{i} = 2.50\,M_\odot$:

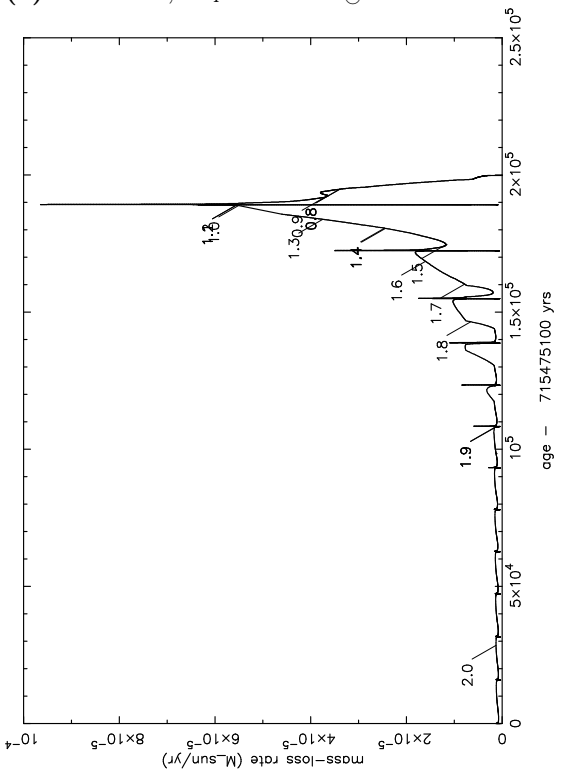

(d) $Z = 0.001$, $M_\mathrm{i} = 2.50\,M_\odot$:

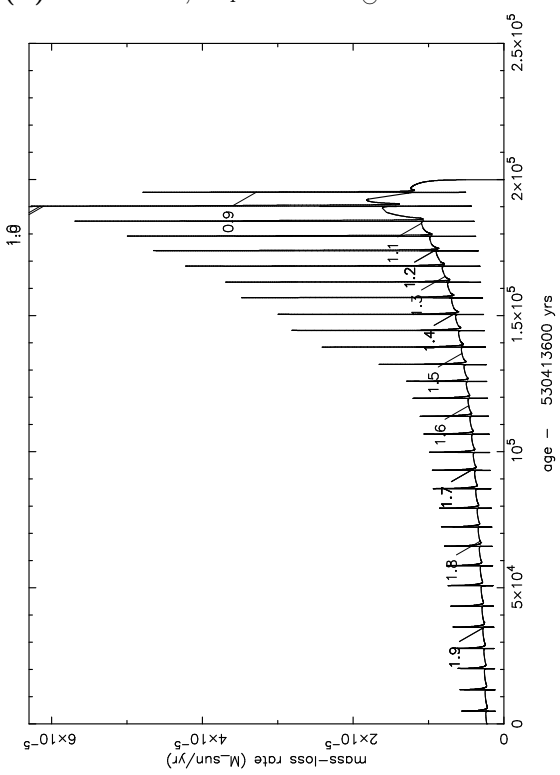

Figure 3.2: Mass loss histories of stars with different initial masses and metallicities.

denser and narrower mass distribution.

3.3 Total mass loss

Another interesting aspect of stellar evolution concerns the masses of white dwarfs which are considered to be the end product of stellar evolution of intermediate-mass stars. The final mass is basically identical with the core mass of the AGB star supposing that the whole envelope is ejected via stellar winds. Therefore we present in the following the integrated or total mass loss of our models.

Figure 3.3 depicts the amount of mass lost by a star with initial mass M_i during its life for the grids of tracks with metallicity (a) $Z = 0.01$ and (b) $Z = 0.001$. In addition the integrated mass loss during the RGB and AGB phase is shown. In both graphs the mass loss of solar stars with respective initial mass are plotted as well for comparison. It can be seen in figure (a) that the total amount of mass loss is virtually the same, but not lower for LMC-like than for solar abundances. However, the contributions lost on the RGB and AGB are shifted, especially for the lower initial masses shown more mass is already lost in the RGB phase. For $Z = 0.001$ figure (b) shows that the total amount of mass lost is almost the same as for solar metallicity for the lower end of initial masses. With higher initial mass though, less material is blown away for SMC-like abundances. Again there is a shift towards higher contribution of the RGB, but less pronounced than in case (a).

3.3.1 Influence of overshooting

The results shown in figure 3.3 are from model calculations with an overshoot parameter $\delta_\mathrm{ov} = 0$ for stars with $M_\mathrm{i} \leq 1.5\,M_\odot$ and $\delta_\mathrm{ov} = 0.12$ with $M_\mathrm{i} > 1.5\,M_\odot$. Table 3.1 lists additional results. As mentioned earlier, core overshooting mainly prolongs the duration of the burning phases, since additional material is mixed into the burning region. As a consequence the stellar ages increase, less so at lower masses (e.g. less than 3% for initial masses less than 1.5 $M_\odot$), but noticeably at higher masses (e.g. 28% for 2 $M_\odot$). Concerning the total mass loss though, it does not have any noteworthy influence, since the values merely change in the second decimal place meaning a general decrease of less than 0.5%.

3.3.2 Initial-final mass relation

Supplementing the discussion of total mass loss, figure 3.4 displays final over initial masses for our grids with heavy element abundances of $Z = 0.02$ (solar), $Z = 0.01$ (∼LMC), and $Z = 0.001$ (∼SMC). The solar values are the ones given in Wachter et al. (2002). While

(a) Models with metallicity $Z = 0.01$:

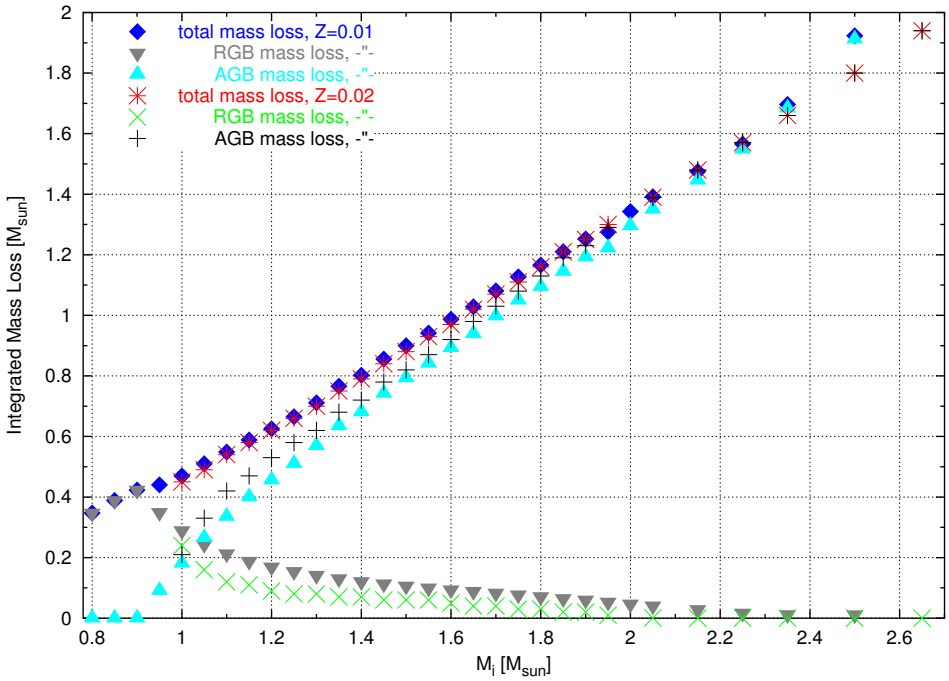

(b) ...and $Z = 0.001$:

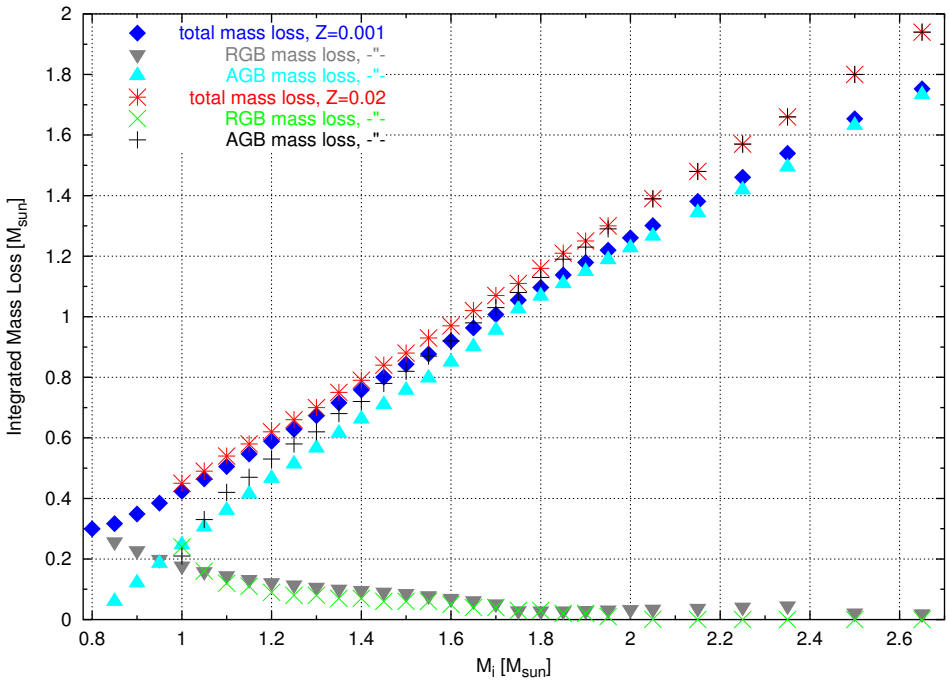

Figure 3.3: Integrated mass loss over initial mass. For each initial mass the total mass loss is shown (blue diamonds) as well as the respective fractions lost on the RGB (cyan) and the AGB (grey). For reference the respective solar values are given as well in both plots (red, green, and black crosses).

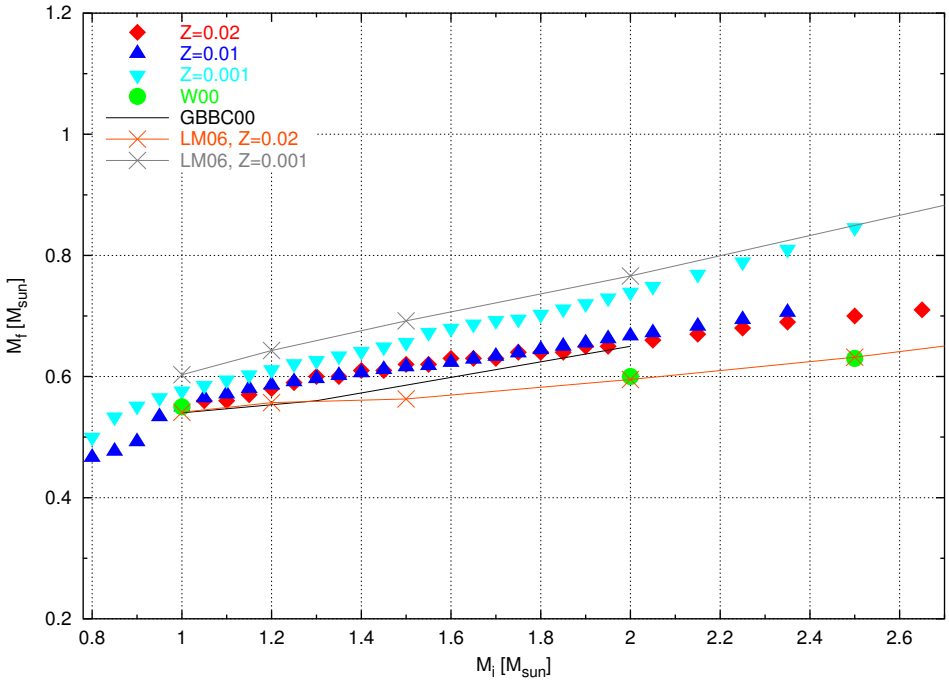

Figure 3.4: Initial–final mass relations of our stellar evolution grids (filled symbols) with $Z = 0.02$ (solar), $Z = 0.01$ (∼LMC), and $Z = 0.001$ (∼SMC). Additional graphs are discribed in section 3.4.

LMC calculations lead to the same initial-final mass relation as solar models, SMC models end their lives with higher final masses.

The additional graphs are some IFMRs we found in the literature. See section 3.4 for a further discussion.

3.4 Discussion

First, a remark concerning the heavy element abundances of the Magellanic Clouds. In this work we assumed metallicities of $Z = 0.008 = 0.4\,Z_\odot$ for the LMC, and $Z = 0.004 = 0.2\,Z_\odot$ for the SMC, since these are accepted as "canonical values" (see e.g. Kerschbaum et al. (2006)). Several other values for their metallicities can be found in the literature as well. Sloan et al. (2006) for example gives the same value for the SMC, but a higher value for the LMC of $Z = 0.5\,Z_\odot = 0.01$, which corresponds exactly to our stellar evolution grid.

Additionally to the initial-final mass relations resulting from our model calculations, figure 3.4 displays others found in the literature to draw a comparison. Unfortunately, a comparison with observational data (semi-empirical IFMRs) is handicapped by the fact that data in the initial mass range presented in this work is rare. Kalirai et al. (2005) for

	Z=0.01				Z=0.001			
	$\delta_{ov} = 0$		$\delta_{ov} = 0.12$		$\delta_{ov} = 0$		$\delta_{ov} = 0.12$	
M_i $[M_\odot]$	M_e $[M_\odot]$	age $[10^9 yr]$	M_e $[M_\odot]$	age $[10^9 yr]$	M_e $[M_\odot]$	age $[10^9 yr]$	M_e $[M_\odot]$	age $[10^9 yr]$
0.70					0.4727	24.24	0.4729	24.33
0.75					0.4866	18.83	0.4868	18.91
0.80	0.4662	23.77	0.4662	23.79	0.5002	14.88	0.4996	14.95
0.85	0.4763	19.02	0.4763	19.04	0.5335	12.06	0.5366	12.14
0.90	0.4919	15.41	0.4911	15.43	0.5515	9.85	0.5596	9.92
0.95	0.5333	12.73	0.5328	12.73	0.5654	8.15	0.5736	8.21
1.00	0.5495	10.53	0.5480	10.54	0.5764	6.82	0.5869	6.88
1.05	0.5646	8.80	0.5589	8.83	0.5857	5.78	0.5957	5.83
1.10	0.5709	7.42	0.5682	7.48	0.5946	4.94	0.6047	4.99
1.15	0.5799	6.31	0.5762	6.40	0.6031	4.26	0.6131	4.32
1.20	0.5856	5.42	0.5836	5.53	0.6117	3.70	0.6214	3.77
1.25	0.5910	4.70	0.5898	4.80	0.6217	3.24	0.6294	3.31
1.30	0.5962	4.11	0.5943	4.19	0.6268	2.86	0.6370	2.93
1.35	0.6015	3.61	0.5993	3.69	0.6344	2.54	0.6446	2.61
1.40	0.6058	3.19	0.6048	3.26	0.6419	2.26	0.6521	2.34
1.45	0.6112	2.85	0.6082	2.92	0.6493	2.03	0.6593	2.11
1.50	0.6158	2.55	0.6132	2.62	0.6567	1.83	0.6665	1.92
1.55	0.6204	2.29	0.6178	2.37	0.6639	1.65	0.6733	1.75
1.60	0.6257	2.07	0.6229	2.16	0.6714	1.50	0.6800	1.61
1.65	0.6307	1.87	0.6283	1.98			0.6880	1.49
1.70	0.6360	1.70	0.6331	1.82			0.6929	1.38
1.75	0.6409	1.55	0.6386	1.67			0.6950	1.35
1.80	0.6461	1.43	0.6441	1.55			0.7032	1.27
1.85	0.6513	1.32	0.6497	1.44			0.7119	1.19
1.90	0.6562	1.22	0.6550	1.37			0.7206	1.10
1.95	0.6612	1.14	0.6620	1.46			0.7301	1.03
2.00	0.6660	1.06	0.6667	1.36			0.7395	0.96
2.05	0.6709	1.00	0.6720	1.27			0.7492	0.90
2.15	0.6808	0.90	0.6828	1.12			0.7692	0.79
2.25	0.6905	0.82	0.6937	0.99			0.7897	0.70
2.35			0.7057	0.88			0.8104	0.62
2.50							0.8463	0.53

Table 3.1: Stellar evolution grids: final masses and ages

example present an initial-final mass relationship from observations of white dwarfs in the open star cluster NGC 2099. Their sample lies in the initial mass range of 2.8 to 3.4 $M_\odot$. Claver et al. (2001) investigated WDs in the open clusters Praesepe, Hyades, and Pleiades with initial masses $M_\mathrm{i} > 2.7\,M_\odot$, and Williams et al. (2004) present results from a spectroscopic analysis of massive WDs in open cluster NGC 2168 with initial masses $M_\mathrm{i} > 4.5\,M_\odot$. Weidemann (2000) though, gives a revised IFMR based on WD observations in open clusters, mainly the Hyades, NGC 3532, and NGC 2516 for initial masses $M_\mathrm{i} = 1 \ldots 7\,M_\odot$. Those values reaching into the considered domain are displayed in figure 3.4 labelled *W00* (green filled circles). The remaining lines represent theoretical IFMRs resulting from other stellar evolution calculations with differing mass-loss descriptions. The curve *GBBC00* reproduces the results of Girardi et al. (2000) for $Z = 0.019$ as displayed in their figure 4. Their evolution models include the mass-loss formalism according to Vassiliadis & Wood (1993) along the TP-AGB. Marigo (2001) combined these Padova models (Girardi et al. 2000) with synthetic TP-AGB models (Marigo et al. 1999, and references therein), resulting in slightly smaller final masses.

Lawlor & MacDonald (2006) present IFMRs for various heavy element abundances (among them $Z = 0.001$, $Z = 0.004$, $Z = 0.01$, and $Z = 0.02$). Their evolution code is also based on Eggleton's, but with different updates concerning the input data. As mass-loss formalism during the AGB phase, they combine the Reimers mass-loss with period-luminosity relations. Their results for $Z = 0.001$, and $Z = 0.02$ are shown in figure 3.4 (*LM06*). Interestingly, their final masses for solar metallicity match exactly the values of Weidemann (2000). For lower metallicities though (especially $Z = 0.001$), their models exhibit lower mass loss than ours, leading to higher final masses.

Chapter 4

Synthetic Populations

Unfortunately, a direct comparison between individual stellar mass loss rates derived from observations (e.g. via CO maser lines or IR data) and from theory can only be done in a few cases where necessary data like stellar masses are known with high enough accuracy. On the other hand, from several surveys a wealth of data is available nowadays which allows for a statistical comparison. Consequently, we present in this chapter synthetic stellar samples calculated on the basis of data given in the previous chapters.

4.1 Generation of synthetic stellar samples

Generally, a stellar sample is nothing but a set of stars with different ages and masses originally born with a distribution in initial masses over some period of time. Thinking the other way around, knowing the evolution of stars dependent on their initial masses (*evolutionary tracks*) in addition to the number of stars born per mass range during a time interval (*stellar creation function*), one can simulate their present day state, i.e. generate a synthetic stellar sample. The stellar creation function (SCF) is usually given per unit logarithmic mass, per unit time and per unit volume or area. The SCF can be separated into the *star formation rate* (or birthrate) giving the average number of stars born per unit time and the *initial mass function*, the number of stars formed in the considered time interval per unit logarithmic mass (and per unit area or volume) as detailed for example by Miller & Scalo (1979).

In the following we describe the way which our program follows to generate a synthetic sample. A schematic illustration can be found in figure 4.1. First, the total number of stars which arise in the considered age interval t_1 and t_2 is determined. It is given by integration of the star formation rate

$$N = \int_{t_1}^{t_2} f_{\mathrm{SFR}}(t)\mathrm{d}t$$

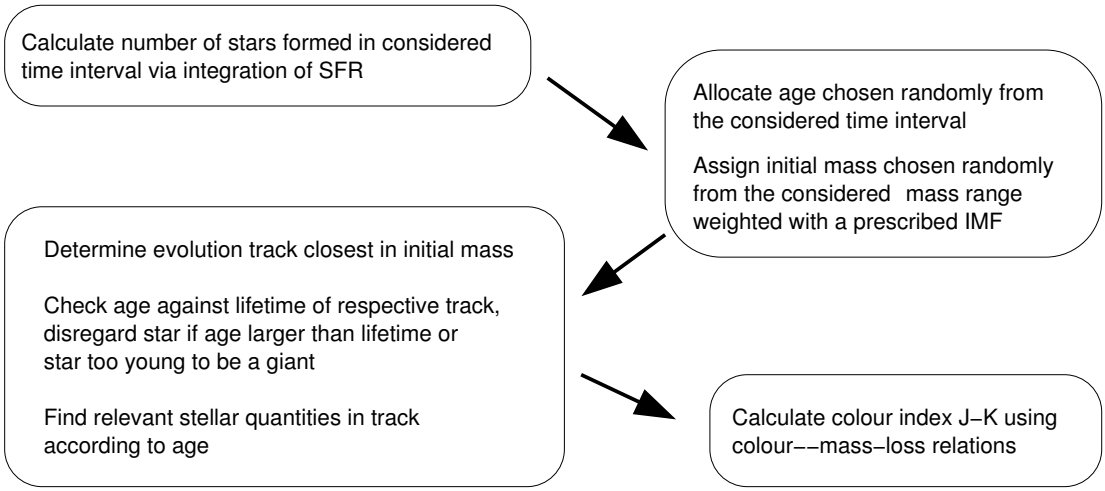

Figure 4.1: Steps to create a synthetic stellar sample.

We allow for a time dependent star formation rate by using

$$f_{\rm SFR}(t) = S_0 \exp(-\frac{\gamma\, t}{10^9})$$

so that positive γ means a SFR increasing with time (t looks back in time, $t = 0$ is the present) and a constant SFR can be considered by setting $\gamma = 0$[1]. An appropriate choice of S_0 determines the number of stars contained in the synthetic sample. Then the following steps are performed for each star. An age within the prescribed time interval is randomly assigned and an initial mass is randomly allocated considering a mass scale weighted with the initial mass function. From the grid of evolutionary tracks the track with the closest initial mass is determined. If the allocated age of the star is larger than the lifetime according to the corresponding track the star is neglected. Since the program aims for a sample of giant stars, the star is as well dropped if it is too young to have reached this stage. For the remaining stars relevant stellar quantities like actual mass, luminosity, mass loss etc. are extracted from the track at appropriate age.

For the distribution over initial mass we use an exponential form for the initial mass function. For our solar grid Schröder & Sedlmayr (2001) found best fits using

$$f_{\rm IMF}(\log_{10}(M_{\rm i})) = \frac{{\rm d}N_\star}{{\rm d}\log_{10}(M_{\rm i})} \propto \begin{cases} M_{\rm i}^{-1.7} & : \quad M_{\rm i} < 1.8 M_\odot \\ M_{\rm i}^{-1.9} & : \quad M_{\rm i} \geq 1.8 M_\odot \end{cases}$$

The possible interval of initial masses is limited to values between 0.7 and 3 $M_\odot$.

In order to compare to observational data in the form of colour–magnitude diagrams, one has to use relations between theoretical quantities like effective temperature, luminosity, or mass loss and observationally accessible ones. To determine the infrared colour

[1] Actually, we describe here the *apparent* SFR which is the *true* SFR minus losses by diffusion, see also section 4.3.1.

index $J-K_S$ (which was for instance measured by the DENIS and 2MASS surveys) we use several relations depending on how far the star is developed. The minimum colour is that of the photosphere, which is relevant when the star has not yet passed through a phase of substantial mass loss. We use the relation between $J-K$ and effective temperature as given by Bessell et al. (1989) which is based on modeling the photospheres of M giants. The relation between the mass-loss rate and the colour index for C-rich AGB stars as given by Schröder et al. (2003) is applied above the critical luminosity. In all other cases $(J-K)$–$\dot{M}$ relations by Le Bertre (1997) for C stars and Le Bertre & Winters (1998) for O-rich stars are used.

Before we present colour-magnitude diagrams of synthetic stellar sample based on our stellar evolution grids given in chapter 3, we would like to make some general remarks on the IMF.

4.2 Implications from IMF & SFR

Often an exponential shape is assumed for the initial mass function $f_{\rm IMF}$ which is either defined as the number of stars per logarithmic mass interval or as the number of stars per mass interval. In that case the two formulations are correlated according to

$$f_{\rm IMF}(\log_{10} M_{\rm i}) = \frac{dN_\star}{d\log_{10} M_{\rm i}} \propto M_{\rm i}^{-a} \Rightarrow f_{\rm IMF}(M_{\rm i}) = \frac{{\rm d}N_\star}{{\rm d}M_{\rm i}} \propto M_{\rm i}^{-(a+1)}$$

Per definition the number of stars in the mass interval M_1 to M_2 is proportional to (for simplicity the index i is dropped here, though M still means the initial mass)

$$\int_{M_1}^{M_2} f_{\rm IMF}(M)\,{\rm d}M = \int_{M_1}^{M_2} m^{-(a+1)}{\rm d}M = \frac{1}{a}(M_1^{-a} - M_2^{-a})$$

For a sample of stars it is useful to normalise the IMF to the total number of stars (i.e. all stars in a considered mass range $M_{\rm lower}$ to $M_{\rm upper}$). Then the above integral naturally gives the percentage of stars with initial mass between M_1 to M_2 of the stellar sample.

The mass contained in the stars amounts to

$$\int_{M_1}^{M_2} f_{\rm IMF}(M)\,M{\rm d}M = \int_{M_1}^{M_2} m^{-a}{\rm d}M = \frac{1}{-a+1}(M_2^{-a+1} - M_1^{-a+1})$$

Defining a mean stellar mass through

$$\overline{M} \equiv \frac{\int_{M_1}^{M_2} f_{\rm IMF}\,M\,{\rm d}M}{\int_{M_1}^{M_2} f_{\rm IMF}\,{\rm d}M} = \frac{a}{a-1}\frac{M_1^{-a+1} - M_2^{-a+1}}{M_1^{-a} - M_2^{-a}}$$

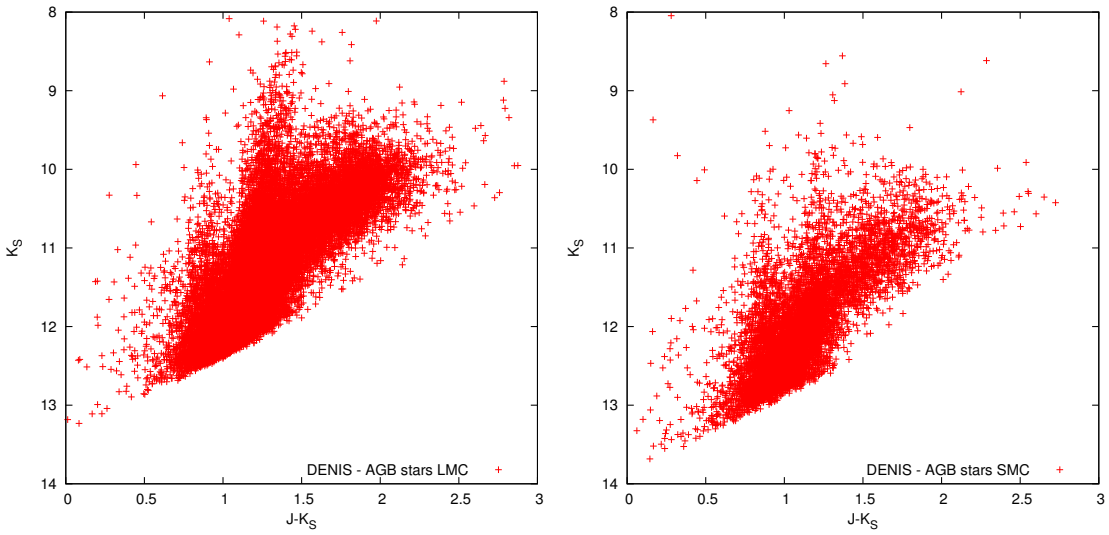

Figure 4.2: $(J - K_S, K_S)$ diagram of AGB stars in the Magellanic Clouds. The data is from the DENIS Catalogue toward Magellanic Clouds (DCMC) (Cioni et al. 2000), the choice of AGB stars is made according to Cioni et al. (2006a,b), and references therein.

one can estimate the present consumption rate of material by $\overline{M} \times f_{\rm SFR}(0)$.

4.3 Colour–magnitude diagrams

As outlined above, colour–magnitude diagrams of complete stellar samples are a possible tool for checking theoretical models with what we are able to see of reality. Figure 4.2 for instance shows broad band observations of giants in the Magellanic Clouds as performed by the Deep Near Infrared Survey of the Southern Sky (DENIS) (Cioni et al. 2000) in K versus $J - K$. A more detailed version of the LMC plot is figure 1 of Cioni et al. (2006a) which flags different types of stars in colour and additionally shows 2MASS data.

4.3.1 Model assumptions

In the following we investigate the dependence of the distribution of our synthetic stellar samples on model assumptions. Figures 4.3 and 4.5 show samples in the $(J - K,\ M_{\rm bol})$ plane for evolutionary tracks with $Z = 0.01$ (a, c) and 0.001 (b, d).

The influence on the slope of the IMF is depicted in figure 4.3. To point out the effect more clearly, we chose $a = 1.5$ and a rather extreme value[2] of 3. In the latter case the

[2]Scalo (1998) reviewed the literature on determinations of the slope of the IMF. He gives a slope of the field star IMF as $a = 1.8$ for $M_{\rm i} = 1.9$-$2.5 \ldots 12\ M_\odot$, and $a = 2.6$ for $M_{\rm i} = 1.4$-$3.5\ M_\odot$. The data on determinations of cluster IMFs he summarises to be $a = 1.5 \ldots 1.8$ for $M_{\rm i} = 1.2 - 10\,M_\odot$, where

number of stars with high initial masses is lower considering samples with the same total number of stars. Therefore, the number density of stars with high $M_{\rm bol}$ is clearly reduced.

Figure 4.4 illustrates this fact. It depicts the locations which stars with different initial masses occupy in the $(J-K)$–$M_{\rm bol}$ plane. The clear spread in bolometric magnitude reflects the fact that the maximum luminosity reached on the AGB increases with initial mass. Stars with initial masses less than one solar mass do not appear in the diagram because they have not yet reached their giant stage.

Concerning the star formation rate figure 4.5 shows the consequences of assuming a non-constant rate in time which one can interpret either directly as a non-constant star formation history or, for instance if a disk population is simulated, in terms of diffusion of low-mass stars. For the synthetic sample the depletion of old stars has the same effect as if these star never had been formed, leading to a lower apparent star formation rate. Since the lifetimes of stars with higher initial masses are considerably shorter (see table 3.1) the depletion has an effect on the lower mass stars with lifetimes longer than the given characteristic diffusion timescale. The displayed samples are calculated to contain the same number of stars. In the case of the higher timescale γ more stars segregate (less stars are born) and are therefore not present in the stellar set. To acquire the same total number at $t = 0$ a higher factor S_0 is needed. As a consequence one finds a higher number density of stars in the upper $M_{\rm bol}$ regime considering equal sized samples, since the ratio of lower-to-higher initial mass stars drops with increasing γ.

4.3.2 Comparison with observational data

Last, we perform a verification of our data with the DENIS data (see figure 4.2). For that purpose bolometric corrections are needed to calculate the K-band magnitude from the bolometric magnitude. We used data by Bessell et al. (1998) by means of approximating their tables 4 and 5 with $BC_K = -0.0007 \times T_{\rm e} + 5.35$. Furthermore, a distance modulus of 18.5 is assumed[3].

Figure 4.6 shows some synthetic samples based on evolutionary tracks with $Z = 0.01$ plotted on top of the DENIS LMC data. Different colours distinguish three types of giants in our samples according to the different determination of the $J-K$ colour index (see section 4.1), RGB (green), O-rich AGB (blue), and C-rich AGB (cyan). All samples are generated with an IMF slope of -1.8, but four different SFRs are applied: constant $\gamma = 0$ (a), $\gamma = 0.2$ (b), $\gamma = 0.5$ (c), and $\gamma = 0.8$ (d). The factor S_0 of the star formation rate is

occasionally values of 2.6 and 2.7 are reported.

[3]Recent determination of the distance modulus of the LMC have been made for instance by Sollima et al. (2006) (18.54 ± 0.15), Keller & Wood (2006) (18.54 ± 0.018), Clement et al. (2005) (18.46 ± 0.08), and Storm et al. (2004) (18.47 ± 0.07)

(a) Synthetic sample based on evolutionary tracks with $Z = 0.01$:

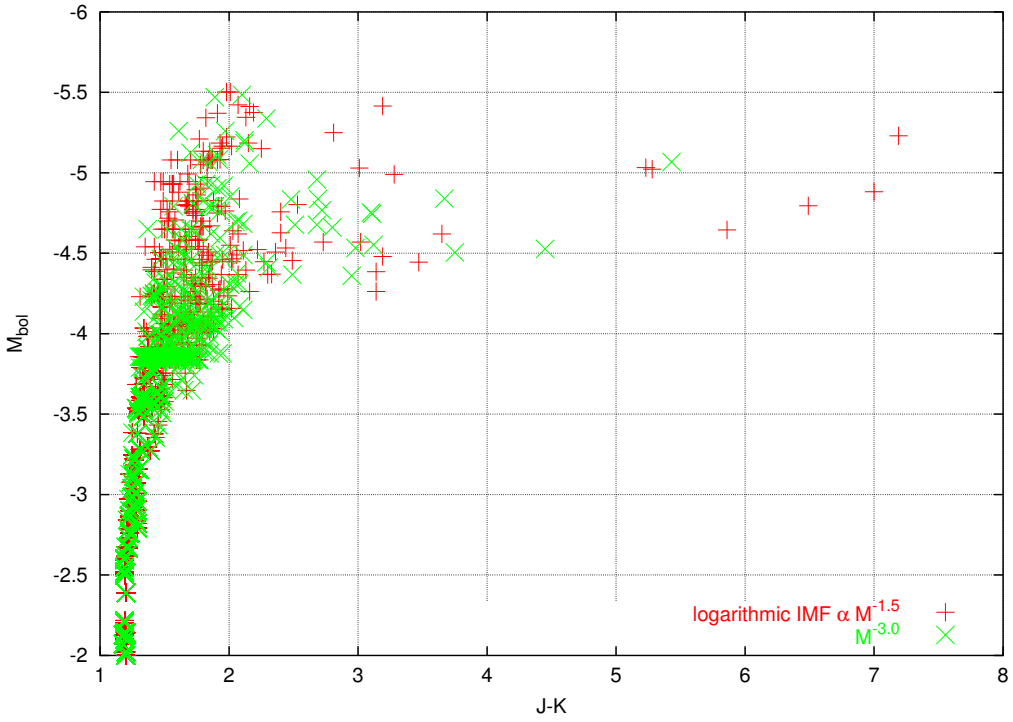

(b) $\ldots Z = 0.001$:

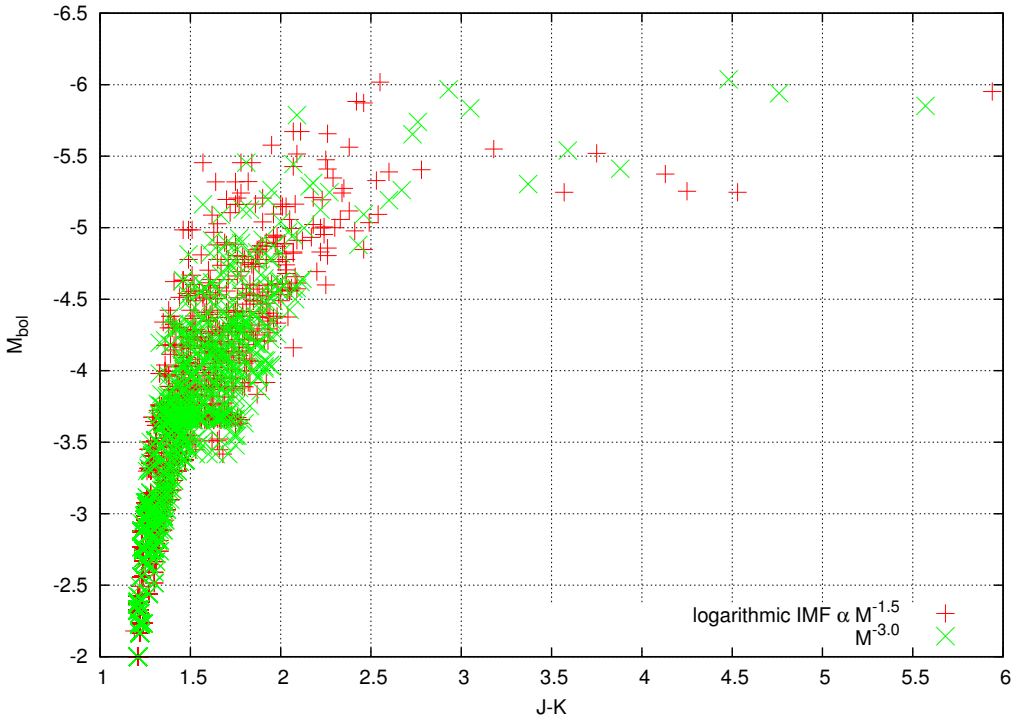

Figure 4.3: Influence of the slope of the IMF on the $(J-K, M_{\mathrm{bol}})$ diagram. Each sample is calculated with a constant SFR and contains 5000 stars.

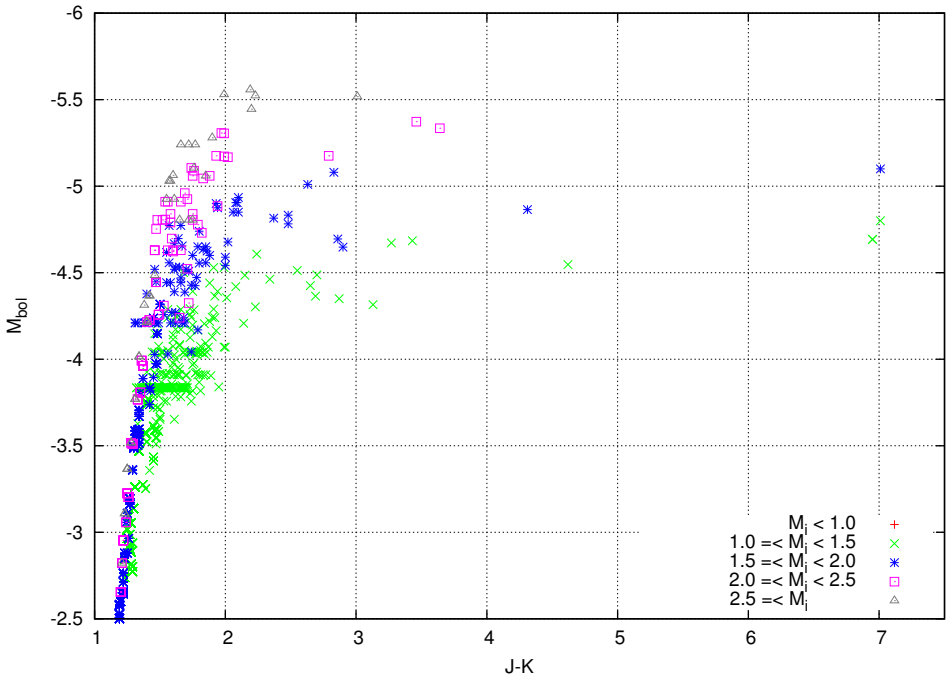

Figure 4.4: Distribution of stars with different initial mass. The sample is calculated on the $Z = 0.01$ grid with constant SFR and an IMF slope of 1.8.

chosen such that the number of stars with $J - K \geq 1.5$ of the DENIS sample (5081 stars) and the synthetic one are equal.

Clearly, the number of more massive stars (around $J - K = 2$ and $K = 10$) in samples (a) and (b) is not high enough to match the observed sample, while in sample (d) too many are present.

4.4 Remarks

All presented synthetic sample are generated with a maximum limit of initial mass of $M_\mathrm{i} = 3.0\,M_\odot$. Therefore (cf. figure 4.4), we miss stars in the higher bolometric magnitude area. Naturally, this influences and complicates quantitative conclusions about the best matching SFR and IMF slope. Spectroscopic determinations of AGB stars hint that O-rich stars are in fact found in the left part of the K / M_bol versus $J-K$ diagram, though. Since hot bottom burning which takes place in stars with $M_\mathrm{i} \gtrsim 4\,M_\odot$ (Herwig 2005) destroys freshly mixed up carbon in the envelope so that these stars remain O-rich despite He shell burning, we expect the number of missed stars in the right part of the diagram to be rather low. A quantitative evaluation has to await an evolutionary grid extended towards higher initial masses, though. An interesting issue closely related to dust-driven winds with O-rich

(a) Synthetic sample based on evolutionary tracks with $Z = 0.01$:

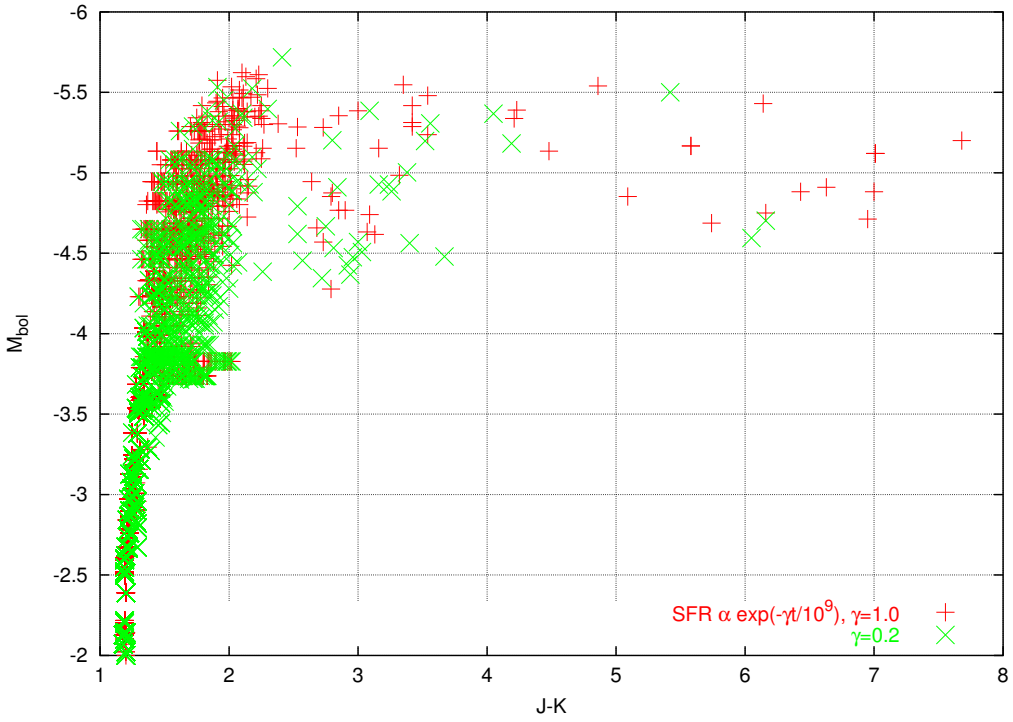

(b) $\ldots Z = 0.001$:

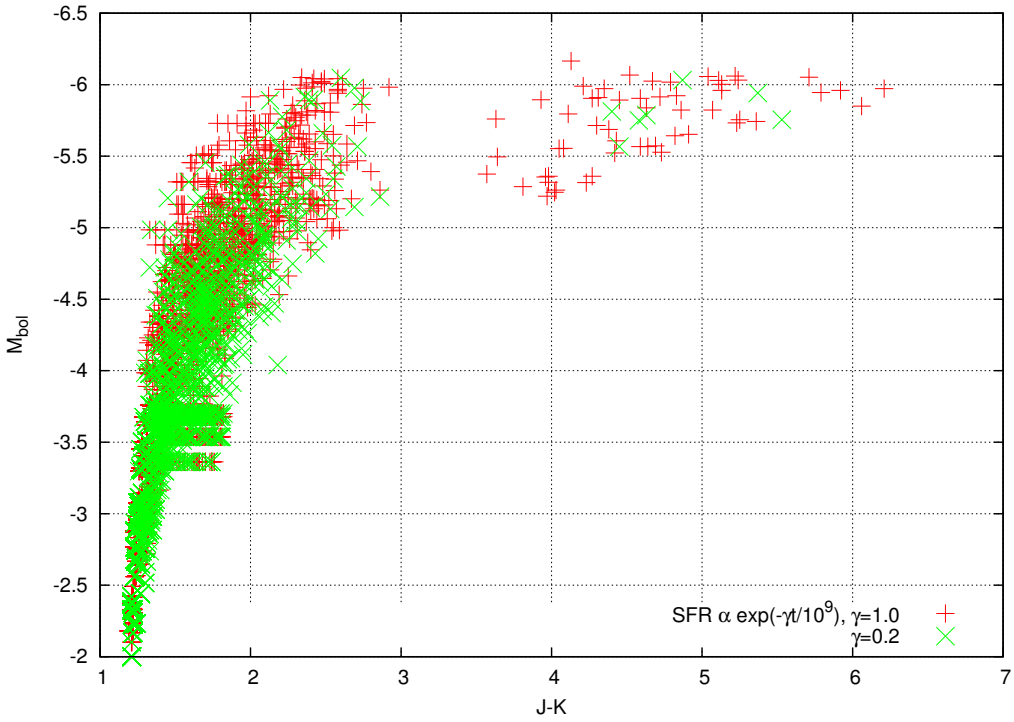

Figure 4.5: Influence of the SFR on the $(J-K,M_{\rm bol})$ diagram. Each sample is calculated with a logarithmic IMF proportional to $M^{-1.8}$ and contains 5000 stars.

(a) $\gamma = 0$:

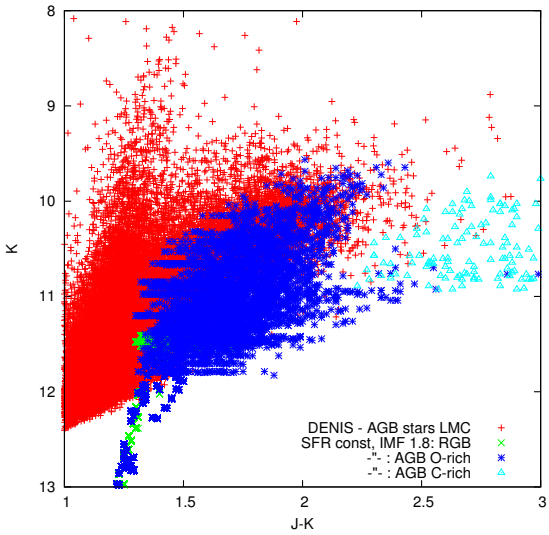

(b) $\gamma = 0.2$:

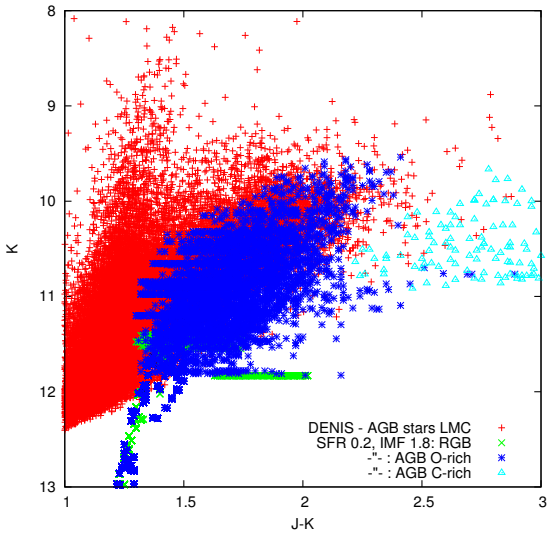

(c) $\gamma = 0.5$:

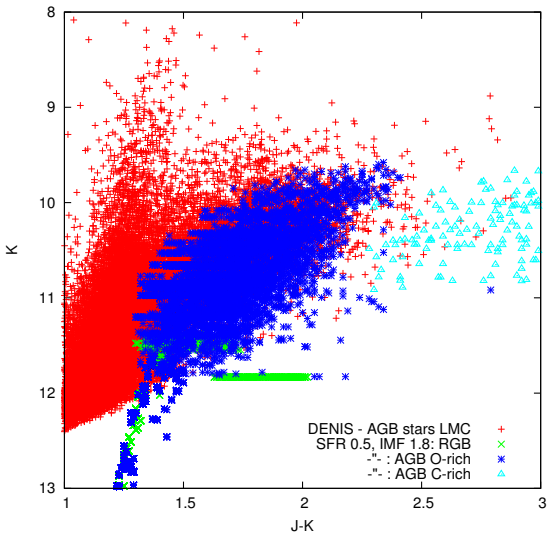

(d) $\gamma = 0.8$:

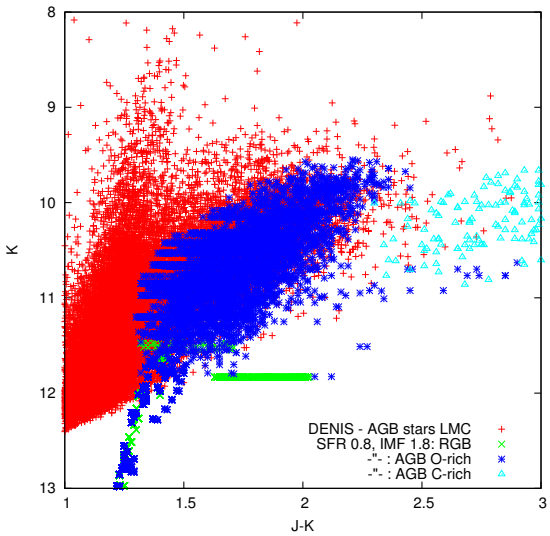

Figure 4.6: Confrontation with DENIS LMC data (same as in figure4.2). Stars of the synthetic sample are colour-coded according to their $J - K$ determination (see text for details).

chemistry which have not been considered in this work.

Our synthetic sample does not contain any stars with $(J-K) < 1.2$ since we take into account the Le Bertre & Winters (1998) $(J-K)$–$\dot{M}$ relation for O-rich stars which results in larger values for mass-loss rates given in our sample.

Furthermore, a precise comparison is complicated by the fact that the DENIS data, as available online, are polluted with foreground stars. Therefore, a very careful filtering of the DENIS sample is necessary before any quantitative conlusions can be drawn. Loup et al. (1999), for instance, who presented a ($J-K$, $M_{\rm bol}$) diagram of RGB and AGB stars of a 0.14 square degree field in the bar of the LMC, employed cross-identification with ISO observations for their DENIS-based sample of LMC giants. Unfortunately, this work has not been continued.

Chapter 5

Summary & Outlook

This work investigates the mass-loss of low- and intermediate mass stars, especially with subsolar metallicities as they are observed in the Magellanic Clouds. Thereby, the main focus lies on the AGB phase, their late evolutionary stage, where these stars lose matter by strong winds with mass-loss rates of up to $\sim 10^{-4}\ M_\odot\ \mathrm{yr}^{-1}$. Dust grains, which form under the favourable conditions in their atmospheres supported by stellar pulsation, play a major role as driving mechanism in that process. Even though dust formation is less efficient at lower metallicity, AGB stars in the Magellanic Clouds are observed to have similar mass-loss rates as their counterparts with solar element abundance!

In earlier works mass-loss induced by dust-driven winds of solar metallicity stars has been explored and quantified. For that purpose, an approximative formula has been derived from a set of time-averaged mass-loss rates of hydrodynamical wind models with carbon-rich element abundances dependent on the stellar parameters – effective temperature T_{eff}, luminosity $L_\star$, and actual mass $M_\star$ – only. In that way, an application to stellar evolution calculations, which do not resolve stellar pulsation per se, is possible. From these computations then result the mass-loss histories of single stars.

First steps towards extending this approach to subsolar metallicities came to the conclusion that dust formation in the hydrodynamical models is not sufficient enough to drive a stable wind. In this work, we overcame this problem by adapting the assumption about the optical depth of the dust shell (see chapter 2). It is reasonable to assume that these shells are optically thick in solar metallicity wind models. With subsolar heavy element abundances though, there is not only less material available for dust formation, but it even turns out that the condensation degree is lower. Therefore, we drop that assumption and allow for at least partial transparency of the envelope to radiation from the stellar photosphere, which finally leads to higher radiation pressure.

We presented and discussed here new sets of hydrodynamical wind models for carbon-rich long-period variables with element abundances as found in the Large and Small Magellanic Cloud, i.e. roughly 1/3 and 1/5 solar, respectively (see appendix A for a list). For

each model set we derived a mass-loss formula which we used then in stellar evolution calculations of appropriate metallicity following the approach previously applied to solar metallicity models.

A comparison of our new subsolar and the corresponding solar element abundance wind models leads to the following new main results:

- With decreasing metallicity Z the final outflow velocity and the dust-to-gas ratio are decreasing.

- There is no clear dependence of the mass-loss rate on Z. Some models with identical other input parameters show higher, some lower values.

- The critical luminosity, which must be reached for a stable wind to develop, is considerably higher at SMC abundances, whereas they are quite alike assuming LMC or solar abundances.

Furthermore, we computed grids of evolutionary tracks using the derived mass-loss formulae. Comparing the total mass loss resulting from these calculations one finds similar results for LMC and solar abundances, but higher final masses in SMC models.

Finally, samples of giant stars have been synthesised on the basis of our evolutionary grids for assumed star formation rates and initial mass functions. They have been confronted with observational data from the DENIS database. There is a general accordance concerning the location and distribution in the ($J-K$, $M_{\rm bol}$) diagram, but a precise comparison is difficult, since the DENIS data available online is polluted with foreground stars and needs to be adjusted. It would be most desirable to have access to refined observational sample like that presented by Loup et al. (1999) who performed a careful by hand selection of AGB stars in the LMC using DENIS data.

A further necessary extension of this work certainly consists in covering the initial mass range beyond $M_{\rm i} = 3\ M_{\odot}$ when calculating stellar evolution with mass loss. Admittedly, this is very time-consuming with the present program version, since the code needs quite some baby-sitting to evolve through the later thermal pulses. Furthermore, at initial masses of more than $\sim$(3.5–4) $M_{\odot}$ our mass-loss description (based on C-stars) is not applicable anymore, because hot bottom burning then destroys the freshly formed carbon so that the star remains oxygen-rich. This is also true when the star is in the early AGB phase, before it undergoes thermal pulses and the third dredge-up which mixes the produced carbon to the stellar surface.

The obvious solution consists in using a mass-loss formula based on wind models for O-rich stars. Indeed, there have been successful investigations of such dust-driven winds

(see Jeong et al. 2003, and references therein), but a systematic examination of the mass-loss dependence on the stellar parameters as needed in the context of stellar evolution is lacking. Only recently, Woitke (2006) came on the basis of his models to the conclusion that the driving mechanism of oxygen-rich AGB stars is still an unsolved puzzle. In other words, a theoretical description for the mass loss of M-stars does not yet exist, so that one would have (still) to refer to semi-empirical formulae.

There remains to mention an interesting open question concerning the mass-loss dependence on metallicity. Our results indicate that the lower the metal abundance the more difficult it is to obtain stable dust-driven winds. So the unanswered question is, if dust-driven winds are a *critical* phenomenon; are they only found above a minimum metallicity?

Appendix A

Lists of Hydrodynamical Wind Models

Tables A.1 and A.2 list all models calculated with the updated version of the code[1] assuming LMC and SMC abundances, respectively. Columns 1–6 contain the input parameters, column 7 the periods over which the averages in colums 8–11 (for an explanation of the quantities see section 2.3.2, and column 12 the model name incl. metallicity.

Table A.1: Collection of LMC models.
Units are M [$M_\odot$], T [K], L [$L_\odot$], $\epsilon_{\mathrm{C/O}}$ [1], P [d], Δv [km s^{-1}], $\langle \dot{M} \rangle$ [$M_\odot$ yr^{-1}], $\langle \alpha \rangle$ [1], $\langle v_{\mathrm{end}} \rangle$ [km s^{-1}], $\langle \rho_{\mathrm{d/g}} \rangle$ [1].

M	T	L	$\epsilon_{\mathrm{C/O}}$	P	Δv	periods	$\langle \dot{M} \rangle$	$\langle \alpha \rangle$	$\langle v_{\mathrm{end}} \rangle$	$\langle \rho_{\mathrm{d/g}} \rangle$	No_type
0.60	2800	8000	1.80	500	5.00	130–150	6.11e-05	3.18	15.01	3.47e-3	lmc103
0.60	2800	10000	1.80	600	5.00	130–150	6.66e-05	2.99	17.23	3.47e-3	lmc101
0.60	3000	10000	1.80	600	5.00	130–150	4.59e-05	4.40	19.88	3.00e-3	lmc102
0.70	2800	8000	1.80	500	5.00	130–150	3.20e-05	4.19	15.83	2.87e-3	lmc93
0.70	2800	10000	1.80	600	5.00	130–150	6.77e-05	2.75	15.27	3.40e-3	lmc91
0.70	3000	8000	1.80	500	5.00	130–150	2.30e-05	4.34	17.88	2.66e-3	lmc94
0.70	3000	10000	1.80	600	5.00	130–150	4.18e-05	4.47	17.94	2.90e-3	lmc92
0.70	3200	8000	1.80	500	5.00	130–150	1.48e-05	5.98	18.69	2.10e-3	lmc109
0.80	2200	5000	1.80	325	5.00	130–150	4.38e-05	1.75	8.82	3.57e-3	lmc79
0.80	2200	5000	1.80	400	5.00	70–90	4.86e-05	1.41	9.62	3.63e-3	a06_lmc
0.80	2200	8000	1.80	500	5.00	130–150	1.13e-04	1.71	12.73	3.71e-3	lmc95
0.80	2200	10000	1.30	650	2.00	70–90	4.11e-05	1.08	7.31	7.66e-4	a02_lmc
0.80	2200	15000	1.30	650	2.00	90–110	1.23e-04	1.48	7.57	7.19e-4	w34_lmc

continued on next page...

[1] as described in chapter 2

Collection of LMC models (continued from previous page)

M	T	L	$\epsilon_{\mathrm{C/O}}$	P	Δv	periods	$\langle\dot{M}\rangle$	$\langle\alpha\rangle$	$\langle v_{\mathrm{end}}\rangle$	$\langle\rho_{\mathrm{d/g}}\rangle$	No_type
0.80	2200	15000	1.80	650	2.00	70–90	1.75e-04	4.24	15.46	3.66e-3	w21_lmc
0.80	2200	15000	1.30	300	5.00	130–150	5.32e-05	0.82	8.62	5.95e-4	w38_lmc
0.80	2200	15000	1.80	300	5.00	70–90	1.20e-04	4.97	16.80	3.75e-3	a01_lmc
0.80	2200	15000	1.30	400	5.00	70–90	1.70e-07	0.06	5.58	2.32e-5	a05_lmc
0.80	2400	5000	1.80	325	5.00	70–90	1.28e-05	1.58	11.78	3.12e-3	a44_lmc
0.80	2400	8000	1.80	500	5.00	70–90	6.49e-05	1.70	11.66	3.47e-3	a32_lmc
0.80	2400	10000	1.80	600	5.00	130–150	9.86e-05	3.07	14.47	3.47e-3	lmc89
0.80	2400	10000	1.30	650	5.00	70–90	4.51e-05	1.09	7.18	7.42e-4	a03_lmc
0.80	2600	5000	1.30	250	5.00	130–150	1.03e-10	0.24	0.41	2.55e-12	w127_lmc
0.80	2600	5000	1.80	325	5.00	190–210	8.46e-06	2.41	13.87	2.54e-3	lmc72
0.80	2600	6000	1.80	400	5.00	130–150	1.73e-05	2.98	15.13	3.01e-3	lmc71
0.80	2600	7500	1.30	300	5.00	–	0000	0000	0000	0000	w113_lmc
0.80	2600	8000	1.80	500	5.00	70–90	3.31e-05	2.60	12.94	3.25e-3	a43_lmc
0.80	2600	10000	1.80	600	5.00	70–90	8.18e-05	1.85	14.45	3.56e-3	a47_lmc
0.80	2800	4000	1.80	400	5.00	110–130	7.57e-06	1.71	13.86	2.06e-3	lmc46
0.80	2800	5000	1.80	325	5.00	130–150	6.07e-06	2.00	17.26	2.58e-3	lmc73
0.80	2800	5000	1.30	400	5.00	130–150	1.45e-09	0.00	1.25	2.15e-8	w52_lmc
0.80	2800	6000	1.80	400	5.00	70–90	1.05e-05	3.12	17.20	2.79e-3	a13_lmc
0.80	2800	8000	1.80	500	5.00	70–90	2.14e-05	3.30	16.69	2.66e-3	a45_lmc
0.80	2800	10000	1.80	600	5.00	130–150	4.45e-05	3.81	16.28	3.26e-3	a35_lmc
0.80	2800	12000	1.80	700	5.00	130–150	6.44e-05	3.36	18.59	3.33e-3	lmc104
0.80	2800	15000	1.50	400	5.00	–	0000	0000	0000	0000	a04t2_lmc
0.80	2800	15000	1.70	400	5.00	70–90	3.51e-05	6.10	18.83	2.01e-3	a04t3_lmc
0.80	2800	15000	1.80	400	5.00	70–90	3.30e-05	3.92	21.04	2.68e-3	a04tst_lmc
0.80	2800	15000	2.50	400	5.00	70–90	4.58e-05	6.03	30.16	7.13e-3	a04t4_lmc
0.80	3000	5000	1.80	325	5.00	190–210	2.04e-06	0.67	16.36	1.80e-3	lmc83
0.80	3000	6000	1.30	400	5.00	130–150	3.03e-08	0.01	3.41	5.68e-4	w47_lmc
0.80	3000	6000	1.80	400	5.00	110–130	5.40e-06	2.50	19.92	2.51e-3	lmc87
0.80	3000	8000	1.80	500	5.00	130–150	1.47e-05	4.99	18.58	2.57e-3	lmc88
0.80	3000	10000	1.30	400	5.00	–	0000	0000	0000	0000	a07_lmc
0.80	3000	10000	1.80	400	5.00	90–110	1.32e-06	0.33	11.87	6.95e-4	a09_lmc
0.80	3000	10000	1.80	600	5.00	130–150	2.70e-05	5.64	17.98	2.58e-3	lmc80
0.80	3000	12000	1.80	700	5.00	130–150	4.12e-05	5.87	17.39	2.37e-3	lmc74
0.80	3200	8000	1.80	500	5.00	130–150	8.72e-06	4.90	19.99	2.08e-3	lmc100
0.80	3200	10000	1.80	600	5.00	130–150	1.65e-05	6.17	19.79	2.07e-3	lmc99
0.90	2200	5000	1.80	325	5.00	130–150	1.78e-05	1.24	8.51	3.43e-3	a37a_lmc
0.90	2200	5000	1.80	600	5.00	70–90	5.08e-05	1.20	8.47	3.76e-3	a37_lmc
0.90	2200	6000	1.80	400	5.00	70–90	3.86e-05	1.65	10.55	3.30e-3	a40_lmc
0.90	2200	8000	1.80	500	5.00	70–90	8.07e-05	1.82	11.20	3.56e-3	a41_lmc
0.90	2400	5000	1.80	325	5.00	130–150	1.28e-05	1.05	11.57	3.53e-3	lmc75

continued on next page...

Collection of LMC models (continued from previous page)

M	T	L	$\epsilon_{\mathrm{C/O}}$	P	Δv	periods	$\langle \dot{M} \rangle$	$\langle \alpha \rangle$	$\langle v_{\mathrm{end}} \rangle$	$\langle \rho_{\mathrm{d/g}} \rangle$	No_type
0.90	2400	6000	1.80	400	5.00	90–110	3.04e-05	1.73	9.79	3.27e-3	lmc60
0.90	2400	8000	1.80	500	5.00	70–90	5.04e-05	2.35	11.89	3.47e-3	a38_lmc
0.90	2400	10000	1.80	600	5.00	110–130	8.83e-05	2.78	13.84	3.52e-3	lmc59
0.90	2600	5000	1.80	325	5.00	190–210	6.76e-06	2.41	14.16	2.79e-3	lmc84
0.90	2600	6000	1.80	400	5.00	170–190	1.26e-05	2.20	15.90	3.14e-3	lmc61
0.90	2600	8000	1.80	500	5.00	90–110	3.09e-05	3.28	14.71	3.04e-3	lmc56
0.90	2600	10000	1.80	600	5.00	90–110	5.40e-05	3.39	14.28	3.52e-3	lmc58
0.90	2800	5000	1.80	325	5.00	170–190	1.73e-06	0.76	12.57	1.74e-3	lmc85
0.90	2800	6000	1.80	400	5.00	130–150	8.01e-06	1.81	16.70	2.35e-3	lmc62
0.90	2800	8000	1.80	500	5.00	70–90	1.69e-05	2.42	18.18	2.86e-3	a39_lmc
0.90	2800	10000	1.80	600	5.00	70–90	3.17e-05	3.23	16.77	2.98e-3	a36_lmc
0.90	3000	5000	1.80	325	5.00	–	0000	0000	0000	0000	lmc76
0.90	3000	6000	1.80	400	5.00	–	0000	0000	0000	0000	lmc63
0.90	3000	7000	1.80	450	5.00	130–150	7.48e-06	3.90	19.64	2.24e-3	lmc66
0.90	3000	8000	1.80	500	5.00	130–150	9.82e-06	4.62	19.38	2.29e-3	lmc64
0.90	3000	10000	1.80	600	5.00	130–150	1.83e-05	5.29	19.51	2.53e-3	lmc65
0.90	3200	6000	1.80	400	5.00	–	0000	0000	0000	0000	lmc98
0.90	3200	7000	1.80	450	5.00	–	0000	0000	0000	0000	lmc105
0.90	3200	8000	1.80	500	5.00	–	0000	0000	0000	0000	lmc97
0.90	3200	9000	1.80	550	5.00	130–150	7.20e-06	5.73	21.36	2.01e-3	lmc110
0.90	3200	10000	1.80	600	5.00	130–150	1.02e-05	5.95	20.62	2.10e-3	lmc96
1.00	2200	6000	1.80	400	5.00	130–150	4.22e-05	1.65	9.54	3.57e-3	lmc77
1.00	2200	8000	1.80	500	5.00	130–150	7.19e-05	2.01	10.72	3.77e-3	lmc78
1.00	2200	10000	1.80	600	5.00	70–90	1.24e-04	2.70	12.50	3.57e-3	a51_lmc
1.00	2200	15000	1.30	400	5.00	–	0000	0000	0000	0000	a08_lmc
1.00	2400	6000	1.80	400	5.00	70–90	1.82e-05	1.59	12.20	3.30e-3	a30_lmc
1.00	2400	7000	1.80	450	5.00	90–110	2.90e-05	1.86	12.11	3.34e-3	lmc54
1.00	2400	8000	1.80	500	5.00	70–90	4.13e-05	1.95	11.28	3.11e-3	a50_lmc
1.00	2400	10000	1.80	600	5.00	70–90	7.68e-05	2.38	12.85	3.35e-3	a29_lmc
1.00	2600	3500	1.80	650	2.00	–	0000	0000	0000	0000	w134_lmc
1.00	2600	5000	1.80	325	5.00	70–90	7.30e-06	2.28	15.06	2.48e-3	a42_lmc
1.00	2600	6000	1.80	400	5.00	70–90	1.41e-05	1.21	15.34	2.61e-3	a48_lmc
1.00	2600	7000	1.80	450	5.00	70–90	1.63e-05	2.68	16.28	3.24e-3	a31_lmc
1.00	2600	8000	1.80	500	5.00	70–90	2.70e-05	2.47	15.23	3.17e-3	lmc55
1.00	2600	10000	1.30	650	2.00	110–130	3.38e-08	0.34	3.28	5.54e-4	w12_lmc
1.00	2600	10000	1.50	650	2.00	90–110	4.00e-07	0.04	4.65	5.56e-4	w11_lmc
1.00	2600	10000	1.80	650	2.00	130–150	1.09e-05	4.54	21.24	2.70e-3	w01_lmc
1.00	2600	10000	1.80	600	5.00	70–90	3.81e-05	3.39	15.96	3.46e-3	a33_lmc
1.00	2600	12000	1.80	700	5.00	70–90	6.75e-05	3.68	14.85	3.55e-3	lmc57
1.00	2800	5000	1.80	325	5.00	110–130	4.47e-06	1.37	15.16	2.23e-3	a12_lmc

continued on next page...

Collection of LMC models (continued from previous page)

M	T	L	$\epsilon_{\mathrm{C/O}}$	P	Δv	periods	$\langle\dot{M}\rangle$	$\langle\alpha\rangle$	$\langle v_{\mathrm{end}}\rangle$	$\langle\rho_{\mathrm{d/g}}\rangle$	No_type
1.00	2800	6000	1.30	400	5.00	130–150	2.90e-07	0.05	4.89	9.10e-4	w96_lmc
1.00	2800	6000	1.80	400	5.00	110–130	6.13e-06	1.63	15.77	1.77e-3	a11_lmc
1.00	2800	7000	1.80	450	5.00	70–90	9.48e-06	2.80	17.97	2.69e-3	lmc53
1.00	2800	8000	1.30	400	5.00	130–150	3.35e-07	0.09	3.54	9.23e-4	w97_lmc
1.00	2800	8000	1.80	400	5.00	70–90	8.90e-06	3.93	20.13	2.74e-3	a10_lmc
1.00	2800	8000	1.80	500	5.00	190–210	1.02e-05	2.65	19.34	2.86e-3	lmc81
1.00	2800	10000	1.30	400	5.00	150–170	3.39e-07	0.27	4.54	4.33e-4	w149_lmc
1.00	2800	10000	1.30	600	5.00	–	0000	0000	0000	0000	lmc52
1.00	2800	10000	1.80	600	5.00	130–150	2.19e-05	4.28	18.14	2.88e-3	lmc82
1.00	2900	5000	1.80	325	5.00	–	0000	0000	0000	0000	lmc107
1.00	3000	5000	1.80	325	5.00	–	0000	0000	0000	0000	lmc86
1.00	3000	6000	1.80	400	5.00	–	0000	0000	0000	0000	lmc68
1.00	3000	7000	1.80	450	5.00	–	0000	0000	0000	0000	lmc70
1.00	3000	8000	1.80	500	5.00	130–150	7.20e-06	3.07	20.81	2.24e-3	lmc67
1.00	3000	10000	1.80	650	2.00	90–110	1.37e-07	0.45	5.19	4.41e-4	w05_lmc
1.00	3000	10000	1.80	600	5.00	70–90	1.21e-05	5.63	20.87	2.65e-3	a34_lmc
1.00	3000	12000	1.80	700	5.00	130–150	2.41e-05	4.89	20.41	2.61e-3	lmc106
1.00	3100	8000	1.80	500	5.00	190–210	4.40e-06	2.92	17.61	1.59e-3	lmc108
1.00	3200	8000	1.80	500	5.00	–	0000	0000	0000	0000	lmc90
1.00	3200	10000	1.80	600	5.00	190–210	6.23e-06	5.13	23.29	1.44e-3	lmc69

Table A.2: Collection of SMC models.
Units are M [$M_\odot$], T [K], L [$L_\odot$], $\epsilon_{\mathrm{C/O}}$ [1], P [d], Δv [km s^{-1}], $\langle\dot{M}\rangle$ [$M_\odot$ yr^{-1}], $\langle\alpha\rangle$ [1], $\langle v_{\mathrm{end}}\rangle$ [km s^{-1}], $\langle\rho_{\mathrm{d/g}}\rangle$ [1].

M	T	L	$\epsilon_{\mathrm{C/O}}$	P	Δv	periods	$\langle\dot{M}\rangle$	$\langle\alpha\rangle$	$\langle v_{\mathrm{end}}\rangle$	$\langle\rho_{\mathrm{d/g}}\rangle$	No_type
0.55	2800	10000	1.80	600	5.00	70–150	9.45e-05	3.26	9.54	2.26e-3	smc64b
0.60	2600	8000	1.80	500	5.00	70–150	6.66e-05	2.30	8.50	1.82e-3	smc79b
0.60	2600	10000	1.80	600	5.00	70–150	1.08e-04	2.62	8.66	2.03e-3	smc82b
0.60	2800	8000	1.80	500	5.00	70–150	3.69e-05	2.53	9.69	1.73e-3	smc80b
0.60	2800	10000	1.80	600	5.00	70–150	7.18e-05	3.02	9.66	2.03e-3	smc62b
0.60	3000	8000	1.80	500	5.00	70–150	3.18e-06	0.25	4.95	7.83e-4	smc81b
0.60	3000	10000	1.80	600	5.00	70–150	4.47e-05	3.30	10.76	1.95e-3	smc63b
0.70	2400	7000	1.80	450	5.00	70–290	2.30e-05	0.29	4.89	2.26e-3	smc54b
0.70	2400	8000	1.80	500	5.00	70–210	5.82e-05	1.19	6.09	2.40e-3	smc10b
0.70	2600	7500	1.80	475	5.00	70–150	3.19e-05	1.75	8.34	2.04e-3	smc77b

continued on next page...

Collection of SMC models (continued from previous page)

M	T	L	$\epsilon_{\mathrm{C/O}}$	P	Δv	periods	$\langle \dot{M} \rangle$	$\langle \alpha \rangle$	$\langle v_{\mathrm{end}} \rangle$	$\langle \rho_{\mathrm{d/g}} \rangle$	No_type
0.70	2600	8000	1.80	500	5.00	70–150	3.74e-05	1.77	8.70	1.90e-3	smc55b
0.70	2800	8000	1.80	500	5.00	70–150	2.37e-05	1.87	9.68	1.68e-3	smc78b
0.70	3000	8000	1.80	500	5.00	70–150	1.36e-06	0.62	4.62	9.07e-4	smc76b
0.70	3000	10000	1.80	600	5.00	70–150	2.68e-05	2.17	11.11	1.68e-3	smc87b
0.80	2400	8000	1.80	500	5.00	70–150	2.70e-05	0.77	6.26	2.44e-3	smc03b
0.80	2400	9000	1.80	550	5.00	70–210	4.58e-05	1.04	6.72	2.42e-3	smc44b
0.80	2400	10000	1.80	600	5.00	150–210	8.37e-06	0.27	4.44	1.60e-3	smc04b
0.80	2500	7000	1.80	450	5.00	70–210	1.34e-05	0.42	6.12	1.99e-3	smc56b
0.80	2500	8000	1.80	500	5.00	70–150	2.90e-05	1.15	7.86	2.04e-3	smc24b
0.80	2500	9000	1.80	550	5.00	70–150	4.34e-05	1.37	7.80	2.34e-3	smc41b
0.80	2500	10000	1.80	600	5.00	70–150	5.38e-05	1.56	8.20	20.8e-3	smc31b
0.80	2600	7000	1.80	450	5.00	70–210	3.78e-06	0.17	4.96	1.79e-3	smc57b
0.80	2600	8000	1.80	500	5.00	70–150	2.75e-05	1.35	8.33	1.95e-3	smc51b
0.80	2600	9000	1.80	550	5.00	70–150	2.77e-05	1.40	8.25	1.80e-3	smc28b
0.80	2600	10000	1.80	600	5.00	70–150	5.14e-05	2.11	9.05	1.87e-3	smc16b
0.80	2700	8500	1.80	525	5.00	70–150	2.40e-05	1.17	8.97	1.82e-3	smc75b
0.80	2700	9000	1.80	550	5.00	70–150	1.93e-05	0.99	8.40	1.76e-3	smc37b
0.80	2700	9500	1.80	575	5.00	70–150	3.41e-05	1.76	9.42	1.71e-3	smc43b
0.80	2700	10000	1.80	600	5.00	70–150	3.65e-05	1.63	9.60	1.87e-3	smc30b
0.80	2800	8000	1.80	500	5.00	70–210	1.91e-06	0.25	4.43	1.07e-3	smc11b
0.80	2800	9000	1.80	550	5.00	70–150	1.95e-05	1.55	9.89	1.57e-3	smc58b
0.80	2800	10000	1.80	600	5.00	70–150	2.88e-05	2.04	10.57	1.75e-3	smc19b
0.80	2800	12000	1.80	700	5.00	70–150	4.69e-05	2.77	10.75	1.89e-3	smc85b
0.80	2900	9000	1.80	550	5.00	150–210	1.96e-06	0.09	4.71	9.27e-4	smc74b
0.80	2900	10000	1.80	600	5.00	70–210	8.14e-06	0.35	7.08	1.19e-3	smc73b
0.80	3000	9000	1.80	550	5.00	70–150	1.21e-06	0.29	4.45	8.20e-4	smc72b
0.80	3000	10000	1.80	600	5.00	70–150	2.10e-06	0.22	5.00	7.60e-4	smc71b
0.80	3000	12000	1.80	700	5.00	70–150	3.19e-05	2.68	11.61	1.79e-3	smc86b
0.90	2500	8500	1.80	525	5.00	70–350	1.75e-05	0.54	6.13	1.99e-3	smc45b
0.90	2500	9000	1.80	550	5.00	70–150	2.93e-05	0.97	8.02	2.12e-3	smc38b
0.90	2500	9500	1.80	575	5.00	110–150	4.12e-05	1.04	7.85	2.23e-3	smc70b
0.90	2500	10000	1.80	600	5.00	70–150	3.97e-05	1.68	8.09	2.16e-3	smc36b
0.90	2600	9000	1.80	550	5.00	70–150	1.76e-05	0.33	7.32	1.95e-3	smc27b
0.90	2600	9500	1.80	575	5.00	70–150	2.82e-05	1.38	9.22	1.88e-3	smc46b
0.90	2600	10000	1.80	600	5.00	70–210	3.03e-05	1.20	8.54	1.82e-3	smc26b
0.90	2700	9000	1.80	550	5.00	70–210	1.77e-06	0.47	4.13	1.23e-3	smc52b
0.90	2700	9500	1.80	575	5.00	70–210	3.05e-06	0.43	4.42	1.16e-3	smc59b
0.90	2700	10000	1.80	600	5.00	70–210	2.17e-05	1.34	8.15	1.72e-3	smc33b
0.90	2800	9000	1.80	550	5.00	150–210	2.33e-06	0.43	4.48	1.14e-3	smc69b
0.90	2800	10000	1.80	600	5.00	70–150	1.92e-05	1.36	9.60	1.56e-3	smc68b

continued on next page...

Collection of SMC models (continued from previous page)

M	T	L	$\epsilon_{\mathrm{C/O}}$	P	Δv	periods	$\langle \dot{M} \rangle$	$\langle \alpha \rangle$	$\langle v_{\mathrm{end}} \rangle$	$\langle \rho_{\mathrm{d/g}} \rangle$	No_type
1.00	2400	11000	1.80	650	5.00	150–350	3.54e-05	0.76	4.82	2.17e-3	smc48b
1.00	2500	10000	1.80	600	5.00	70–210	1.79e-05	0.61	6.23	1.82e-3	smc32b
1.00	2500	11000	1.80	650	5.00	70–150	3.89e-05	1.07	7.58	2.49e-3	smc49b
1.00	2600	10000	1.80	600	5.00	70–150	1.19e-05	0.44	5.85	1.41e-3	smc05b
1.00	2600	11000	1.30	650	5.00	150–210	5.86e-07	0.11	3.30	9.26e-5	smc53b1
1.00	2600	11000	1.80	650	5.00	70–150	3.69e-05	1.26	8.56	1.82e-3	smc53b
1.00	2700	10000	1.80	600	5.00	70–410	1.63e-05	0.82	7.94	1.68e-3	smc67b
1.00	2700	11000	1.80	650	5.00	70–150	4.53e-06	0.03	4.60	1.22e-3	smc84b
1.00	2800	10000	1.80	600	5.00	70–210	3.05e-06	0.28	4.79	1.32e-3	smc20b
1.00	2800	11000	1.80	650	5.00	150–290	7.99e-06	0.34	5.68	1.05e-3	smc60b
1.00	3000	11000	1.80	650	5.00	70–150	5.75e-06	0.01	5.11	1.00e-3	smc61b
1.10	2500	10000	1.80	600	5.00	70–350	1.97e-05	0.54	6.33	1.95e-3	smc65b
1.10	2500	11000	1.80	650	5.00	150–290	3.45e-05	1.06	6.99	2.02e-3	smc83b
1.10	2600	11000	1.80	650	5.00	70–150	1.93e-05	0.46	7.68	1.63e-3	smc66b

Bibliography

Alexander, D. R., Ferguson, J. W., ApJ 437, 879

Alvarez, R., Mennessier, M.-O., 1997, A&A 317, 761

Arndt, T. U., Fleischer, A. J., Sedlmayr, E., 1997, A&A 327, 614

Bergeat, J., Chevallier, L., 2005, A&A 429, 235

Bessell, M. S., Brett, J. M., Scholz, M., Wood, P. R., 1989, A&AS 77, 1

Bessell, M. S., Castelli, F., Plez, B., 1998, A&A 333, 231

Bowen, G. H., 1988, ApJ 329, 299

Busso, M., Gallino, R., Wasserburg, G. J., 1999, ARA&A 37, 239

Caughlan, G. R., Fowler, W. A., Harris, M. J., Zimmerman, B. A., 1985, Atomic Data & Nuclear Data Tables 35, 198

Caughlan, G. R., Fowler, W. A., 1988, Atomic Data & Nuclear Data Tables 40, 284

Cioni, M.-R. L., Marquette, J.-B., Loup, C. Azzopardi, M., Habing, H. J., et al., 2001, A&A 377, 945

Cioni, M.-R. L., Girardi, L., Marigo, P., Habing, H. J., 2006, A&A 448, 77

Cioni, M.-R., Loup, C., Habing, H. J., Fouque, P., Bertin, E., 2000, A&AS 144, 235

Cioni, M.-R. L., Girardi, L., Marigo, P., Habing, H. J., 2006, A&A 452, 195

Claver, C. F., Liebert, J., Bergeron, P., Koester, D., 2001, ApJ 563, 987

Clement, C. M., Xu, X., Muzzin, A. V.,2005, Bull. AAS 37, 1364

Eggleton, P. P., 1971, MNRAS 151, 351

Eggleton, P. P., 1972, MNRAS 156, 361

Eggleton, P. P., 1973, MNRAS 163, 279

Eggleton, P. P., 1983, MNRAS 204, 449

Fleischer, A. J., Gauger, A., Sedlmayr, E., 1992, A&A 266, 321

Fleischer, A. J., 1994, *Hydrodynamics and Dust Formation in the Circumstellar Shells of Miras and Long-Period Variables*, PhD thesis, Technische Universität, Berlin, Germany

Gail, H.-P., Sedlmayr, E., 1988, A&A 206, 153

Gauger, A., Gail, H.-P., Sedlmayr, E., 1990, A&A 235, 345

Girardi, L., Bressan, A., Bertelli, G., Chiosi, C., 2000, A&AS 141, 371

Groenewegen, M. A. T., Whitelock, P. A., 1996, MNRAS 281, 1347

Habing, H. J., 1996, A&ARv 7, 97

Habing, H. J., Olofsson, H., (eds.), 2004, "Asymptotic Giant Branch Stars", Springer-Verlag, New York

Han, Z., Podsiadlowski, P., Eggleton, P. P., MNRAS 270, 121

Hashimoto, O., 1995, ApJ 442, 286

Helling, Ch., Arndt, T. U., Sedlmayr, E., 2002, in: ASP Conf. Ser. 259: IAU Colloq. 185: Radial and Nonradial Pulsations as Probes of Stellar Physics, (eds.) Aerts, C., Bedding, T. R., Christensen-Dalsgaard, J., 546

Helling, C., Winters, J. M., Sedlmayr, E., 2000, A&A 358, 651

Herwig, F., 2005, ARA&A 43, 435

Iben, Jr., I., Renzini, A., 1983, ARA&A 21, 271

Itoh, N., Adachi, T., Nakagawa, M., Kohyama, Y., Munakata, H., 1989, ApJ 339, 354 (erratum 360, 741)

Itoh, N., Mutoh, H., Hikita, A., Kohyama, Y., 1992, ApJ 395, 622 (erratum 404, 418)

Jeong, K. S., Winters, J. M., Le Bertre, T., Sedlmayr, E., 2003, A&A 407, 191

Kalirai, J. S., Richer, H. B., Reitzel, D., Hansen, B. M. S., Rich, R. M., Fahlman, G. G., Gibson, B. K., von Hippel, T., 2005, ApJ 618, L123

Keller, S. C., Wood, P. R., 2006, ApJ 642, 834

Kerschbaum, F., Olofsson, H., Wing, R., (eds.), in prep., Proc. *Why Galaxies Care About AGB Stars*, 7–11 August 2006, Vienna, Austria

Lafon, J.-P. J., Berruyer, N., 1991, A&ARv 2, 249

Lamers, H. J. G. L. M., Casinelli, J. P., 1999, An introduction to stellar winds, Cambridge University Press

Lawlor, T. M., MacDonald, J., 2006, MNRAS 371, 263

Le Bertre, T., 1997, A&A 324, 1059

Le Bertre, T., Winters, J. M., 1998, A&A 334, 173

Loup, C., Josselin, E., Cioni, M.-R., Habing, H. J., Blommaert, J. A. D. L., et al., 1999, in: IAU Symp. 191: Asymptotic Giant Branch Stars, (eds.) Le Bertre, T., Lèbre, A., Waelkens, C., 561

Marigo, P., Girardi, L., Bressan, A., 1999, A&A 344, 123

Marigo, P., 2001, A&A 370, 194

Matsuura, M., Zijlstra, A. A., van Loon, J. T., Yamamura, I., Markwick, A. J., Whitelock, P. A., Woods, P. M., Marshall, J. R., Feast, M. W., Waters, L. B. F. M., 2005, A&A 434, 691

Miller, G. E., Scalo, J. M., 1979, ApJS 41, 513

Olofsson, H., Carlström, U., Eriksson, K., Gustafsson, B., Willson, L. A., 1990, A&A 230, L13

Olofsson, H., Bergman, P., Lucas, R., Eriksson, K., Gustafsson, B., Bieging, J. H., 2000, A&A 353, 583

Pols, O. R., Tout, C. A., Eggleton, P. P., Han, Z., 1995, MNRAS 274, 964

Pols, O. R., Schröder, K.-P., Hurley, J. R., Tout, C. A., Eggleton, P. P., 1998, MNRAS 298, 525

Preibisch, T., Ossenkopf, V., Yorke, H. W., Henning, T., 1993, A&A 279, 577

Reimers, D., 1975, MSRSL 8, 369

Renzini, A., 1981, in: Physical processes in red giants, Proc. 2nd workshop, (eds.) Iben Jr., I., Renzini, A., Reidel Publishing, Dordrecht, Holland

Richtmyer, R. D., Morton, K. W., 1967, Difference methods for initial-value problems, John Wiley & Sons, New York, 2nd ed.

Rogers, F. J., Iglesias, C. A. 1992, ApJS 79, 507

Scalo, J., 1998, in: ASP Conf. Ser. 142: The Stellar Initial Mass Function, (eds.) Gilmore, G., Howell, D., 201

Schröder, K.-P., Cuntz, M., 2005, ApJ 630, L73

Schröder, K.-P., Eggleton, P. P., 1996, RvMA 9, 221

Schröder, K.-P., Pols, O. R., Eggleton, P. P. 1997, MNRAS 285, 696

Schröder, K.-P., Sedlmayr, E., 2001, A&A 366, 913

Schröder, K.-P., Wachter, A., Winters, J. M., 2003, A&A 398, 229

Schirrmacher, V., Woitke, P., Sedlmayr, E., 2003, A&A 404, 267

Sedlmayr, E., 1994, in: IAU Colloq. 146: Molecules in the stellar environment, (ed.) Jørgensen, U. G., Springer-Verlag Berlin, 163

Sedlmayr, E., Winters, J. M., 1991, Dust in the shells of cool giants and supergiants, in: Stellar Atmospheres: Beyond Classical Models, (eds.) Crivellari, L., Hubeny, I., Hummer, D. G., 397–408, Kluwer Academic Publishers

Sloan, G. C., Devost, D., Bernard-Salas, J., Wood, P. R., Houck, J. R., 2006, ApJ 638, 472

Sollima, A., Cacciari, C., Valenti, E., 2006, MNRAS 372, 1675

Storm, J., Carney, B. W., Gieren, W. P., Fouqué, P., Latham, D. W., Fry, A. M., 2004, A&A 415, 531

Tscharnuter, W. M., Winkler, K.-H., 1979, Comp. Phys. Comm. 18, 171

Unno, W., Kondo, M., 1976, PASJ 28, 347

van Loon, J. T., Cioni, M.-R. L., Zijlstra, A. A., Loup, C., 2005, A&A 438, 273

Vassiliadis, E., Wood, P. R., 1993, ApJ 413, 641

Wachter, A., Schröder, K.-P., Winters, J. M., Arndt, T. U., Sedlmayr, E., 2002, A&A 384, 452

Wallerstein, G., Knapp, G. R., 1998, ARA&A 36, 369

Weidemann, V., 2000, A&A 363, 647

Williams, K. A., Bolte, M., Koester, D., 2004, ApJ 615, L49

Willson, L. A., 2000, ARA&A 38, 573

Winters, J. M., 1994, *Internal structure and optical appearance of circumstellar dust shells around cool carbon giants*, PhD thesis, Technische Universität, Berlin, Germany

Winters, J. M., Fleischer, A. J., Gauger, A., Sedlmayr, E., 1994, A&A 290, 623

Winters, J. M., Fleischer, A. J., Le Bertre, T., Sedlmayr, E., 1997, A&A 326, 305

Winters, J. M., Le Bertre, T., Jeong, K. S., Helling, Ch., Sedlmayr, E., 2000, A&A 361, 641

Woitke, P., 2006, A&A 460, L9

Danksagung – Acknowledgement

"Sooo, jetzt hab' ich das tatsächlich geschafft!"
Eine Menge Leute haben dazu beigetragen, dass ich das nun sagen kann. An alle ein dickes Danke!

Es war mir eine große Freude, diese Arbeit am Zentrum für Astronomie und Astrophysik anfertigen zu können. Herr Sedlmayr, vielen Dank für die wissenschaftliche und auch menschliche Unterstützung, mit der Sie mich über die Jahre hinweg gefördert haben.

Liebe Kollegen und Studis, sorgt bitte weiterhin für solch ein fröhliches, offenes Miteinander. Es half, mich gelegentlich auch mal über die Schlechtigkeit der Welt ausjammern zu dürfen. Mein Beileid an alle, die das ertragen haben. Die vielen Gespräche und Diskussionen über Freudiges und Interessantes halfen umso mehr. Danke für jeden neuen Einblick und andere Sichtweise.

Beate, Vasco, Micha, Matthias, Jan, Claudia, Sime, und die gelegentlichen Mitgucker, mit euch (und etlichen kleinen Fäßchen) kann man doch jedem Film etwas abgewinnen[1].

Beate und Micha, Danke fürs letzte Korrekturlesen der Arbeit und fürs Probehören des Vortrags! Bunte Bildchen sind in der Tat nicht das Schlechteste...

Uwe, Herrscher über Mordor & streifen-produzierende Farbdrucker, Danke für die in Rat und Tat erfolgte Hilfe (nicht nur) bei Computerfragen.

Karin, Danke für die aufmunternden und ermutigenden Worte zur rechten Zeit.

Großes Lob verdienen außerdem meine Kooperationspartner. Sie haben mich mit ihren Einführungen auf den Weg gebracht, waren immer bereit, meine Fragen zu beantworten und reagierten prompt, wenn es mal wieder etwas gegenzulesen galt.

Klaus-Peter, durch deinen Hinweis auf das EU-Stipendium in Brighton hast du letztlich den Stein ins Rollen gebracht. Du hast mir dadurch ein wissenschaftlich interessantes und persönlich erlebnisreiches Jahr beschert und außerdem maßgeblich zum Gelingen des DFG-Antrags und somit meiner anschließenden Anstellung am ZAA beigetragen. Herzlichen Dank!

Jan Martin, ich hatte großartige Zeiten mit dir in Brighton, Paris, Grenoble und Berlin. Es war jede Menge Spaß dabei gepaart mit einer ordentlichen Portion Sarkasmus und der einen oder anderen Prise Zynismus. Die Atmosphäre war also wunderbar, um bei den Besuchen auch immer eine Menge zu lernen. Vielen Dank dir und auch Beatrice dafür, dass ihr mich mehrmals als Gast aufgenommen und dabei ausgiebig an der Reduzierung eurer flüssigen Vorräte beteiligt habt!

[1] Und bald halte ich euch auch beim Spielen nicht mehr auf... ☺

Dann waren da noch Freunde und Familie, die mitgefühlt, mitgelitten und zuletzt sich mitgefreut haben. Danke, Danke, DANKE!

Mom & Paps, die Überraschung ist euch gelungen... Was soll ich sagen? Danke für alles!

Holger, ohne dich wäre mein Schlafmangel wohl ins Unermessliche erwachsen. Danke fürs Durchhalten und entspannende Rückenkraulen.

Liam and Neil, thank you for great times in England, the effort of improving my English in general, and particularly for checking chapters of this thesis without being too picky.

This work has been supported by DEUTSCHE FORSCHUNGSGEMEINSCHAFT, DFG grant SE 420/22. My stay at the University of Sussex at Falmer, Brighton, UK has been financed by a Marie Curie Fellowship of the European Community programme HUMAN POTENTIAL under the contract number HPMT-CT-2000-00096.

Der Vollständigkeit halber:

Prof. Dr. Erwin Sedlmayr, Dr. Beate Patzer, Dipl.-Phys. Vasco Schirrmacher, Dr. Michael Hegmann, Dipl.-Phys. cand. Matthias Wendt, Dipl.-Math. Jan Bolte, Dipl.-Phys. Claudia Dreyer, Dipl.-Phys. Sime Pervan, Dipl.-Phys. Uwe Bolick, Dipl.-Phys. Karin Sedlmayr, Dr. habil. Klaus-Peter Schröder, Dr. Jan Martin Winters, Dr. Beatrice Wenk, Olga Wachter, Karl Wachter, Holger Räsenhöft, Dr. Neil McNair, Dr. Liam O'Connell